Geophysical Journal International

Geophys. J. Int. (2013) **192,** 537–556 doi: 10.1093/gji/ggs051

Flow throughout the Earth's core inverted from geomagnetic observations and numerical dynamo models

Julien Aubert

Dynamique des Fluides Géologiques, Institut de Physique du Globe de Paris, Sorbonne Paris Cité, Université Paris-Diderot, UMR 7154 CNRS, 1 *rue Jussieu,* F-75005 *Paris, France. E-mail: aubert@ipgp.fr*

Accepted 2012 October 30. Received 2012 October 22; in original form 2012 September 4

SUMMARY

This paper introduces inverse geodynamo modelling, a framework imaging flow throughout the Earth's core from observations of the geomagnetic field and its secular variation. The necessary prior information is provided by statistics from 3-D and self-consistent numerical simulations of the geodynamo. The core method is a linear estimation (or Kalman filtering) procedure, combined with standard frozen-flux core surface flow inversions in order to handle the non-linearity of the problem. The inversion scheme is successfully validated using synthetic test experiments. A set of four numerical dynamo models of increasing physical complexity and similarity to the geomagnetic field is then used to invert for flows at single epochs within the period 1970–2010, using data from the geomagnetic field models CM4 and gufm-sat-Q3. The resulting core surface flows generally provide satisfactory fits to the secular variation within the level of modelled errors, and robustly reproduce the most commonly observed patterns while additionally presenting a high degree of equatorial symmetry. The corresponding deep flows present a robust, highly columnar structure once rotational constraints are enforced to a high level in the prior models, with patterns strikingly similar to the results of quasi-geostrophic inversions. In particular, the presence of a persistent planetary scale, eccentric westward columnar gyre circling around the inner core is confirmed. The strength of the approach is to uniquely determine the trade-off between fit to the data and complexity of the solution by clearly connecting it to first principle physics; statistical deviations observed between the inverted flows and the standard model behaviour can then be used to quantitatively assess the shortcomings of the physical modelling. Such deviations include the (i) westwards and (ii) hemispherical character of the eccentric gyre. A prior model with angular momentum conservation of the core–mantle inner-core system, and gravitational coupling of reasonable strength between the mantle and the inner core, is shown to produce enough westward drift to resolve statistical deviation (i). Deviation (ii) is resolved by a prior with an hemispherical buoyancy release at the inner-core boundary, with excess buoyancy below Asia. This latter result suggests that the recently proposed inner-core translational instability presently transports the solid inner-core material westwards, opposite to the seismologically inferred long-term trend but consistently with the eccentricity of the geomagnetic dipole in recent times.

Key words: Inverse theory; Dynamo: theories and simulations; Rapid time variations.

1 INTRODUCTION

It has long been recognized that the variation of the Earth's magnetic field in time (known as the secular variation) provides a powerful probe to infer the flow of electrically conducting fluid at the top of the outer core, hence imaging part of the motion responsible for the geodynamo. The first decades of active research on the topic, summarized in the review of Bloxham & Jackson (1991), concentrated on laying down the theoretical bases and numerical tools to handle the large amount of underdetermination of this core surface flow problem. At this point it was acknowledged that, on account of the fact that the mantle is mostly insulating and the core highly conductive, magnetic field measurements can be continued downward from the Earth surface down to the core surface, but not further below, thus largely hindering our ability to image flow throughout the core. Such an achievement would certainly be highly desirable to advance the general understanding of the geodynamo, evaluate the state of its couplings with the adjacent layers (the inner core and the mantle), and properly initialize geomagnetic data assimilation algorithms (see Fournier *et al.* 2010, for a review). Over the last two decades, the improved understanding of the magnetohydrodynamics

of rapidly rotating fluids has brought a number of interesting dynamic assumptions which could help to circumvent the issue of downward continuing the velocity field from below the core surface. Recently, Jault (2008) observed that rapid, diffusionless dynamic phenomena developing within a rapidly rotating fluid on the Alfvén wave timescale

$$\tau_A = \frac{D(\mu\rho)^{1/2}}{B} \tag{1}$$

are remarkably columnar (invariant in the direction of the Earth's rotation axis) if τ_A is much longer than the Earth inverse rotation rate $\tau_\Omega = 1/\Omega$ (here D, μ and ρ are, respectively, the outer-core thickness, magnetic permeability and density, and B is the typical magnetic field strength within the outer core). Recent independent estimates of B favouring a strength of several milliteslas (Aubert *et al.* 2009; Buffett 2010), yield τ_A on the order of a few years, possibly consistent with a 6-yr oscillation in the length-of-day (l.o.d.) variations (Gillet *et al.* 2010) and the ratio $\lambda = \tau_\Omega/\tau_A$ (the Lehnert number) on the order of $\lambda \approx \times 10^{-4}$. On that basis, it has been proposed (Pais & Jault 2008; Gillet *et al.* 2009) that for flow on interannual to decadal timescales, a columnar downward continuation of the velocity field can be performed within the quasi-geostrophic framework formulated four decades ago (Busse 1970) and which has found increasingly compelling numerical implementations from 1990 onwards (see a recent review by Finlay *et al.* 2010). These inversions account for the lateral motion of core–mantle boundary geomagnetic flux patches (e.g. Bloxham & Jackson 1991; Holme 2007; Finlay *et al.* 2010) by revealing a planetary-scale, westwards, columnar eccentric gyre moving closer to the core–mantle boundary in the Atlantic Hemisphere, and recessing towards the inner-core boundary in the Pacific Hemisphere, where evidence of geomagnetic westward drift is more elusive. Such a gyre is intriguing because it does not have an equivalent in the solutions so far produced by 3-D direct numerical dynamo modelling. The gyre is robustly obtained over the last half century (Gillet *et al.* 2009), and may have been stable throughout the historical geomagnetic period, for as long as the westward drift itself (Finlay *et al.* 2010). Such a persistence naturally raises the concern of the validity of the quasi-geostrophic framework for timescales much longer than τ_A, particularly the core overturn time $\tau_U = D/U$, where U is a typical core flow velocity. On these timescales, thermal and magnetic anomalies have enough time to rearrange such as to respect thermal and magnetic wind equilibria which can disrupt quasi-geostrophy (e.g. Aubert 2005). One of the most widely conjectured manifestations of this effect is for instance the existence of polar vortices (Olson & Aurnou 1999; Sreenivasan & Jones 2005) within the tangent cylinder (the axial cylinder encircling the inner core).

Interestingly, modern 3-D, self-consistent simulations of convective dynamos seem to generally have strengths and weaknesses nicely complementing quasi-geostrophic models. Their large-scale magnetic field output can be strikingly similar to the geomagnetic field (Christensen *et al.* 2010) provided that three timescales are brought in reasonable proportion with respect to their Earth counterparts: the core overturn time τ_U, the Earth inverse rotation rate τ_Ω and the magnetic dissipation time $\tau_\eta = D^2/\eta$, where η is the magnetic diffusivity of the outer-core liquid iron. Furthermore, numerical dynamos respecting these conditions also adequately render a surprisingly broad temporal spectrum of geomagnetic variations (Christensen *et al.* 2012; Olson *et al.* 2012) around the overturn timescale τ_U, thus suggesting that a large part of the temporal geomagnetic power spectrum is affected by advective transport phenomena. Unfortunately, although the magnetic Reynolds number $Rm = \tau_\eta/\tau_U$ can be brought to the correct value pertaining to the Earth's core of about 1000, the magnetic Ekman number $E_\eta = \tau_\Omega/\tau_\eta$ is currently limited to values of about 10^{-5} while the core value is on the order of 10^{-9} (see Christensen 2011, for a recent review). As a consequence, numerical dynamos presently considered as 'Earth-like' still lack the short timescale (interannual to decadal) rotational dynamics precisely targeted by quasi-geostrophic models. Another connected question is whether the spatial and temporal similarity of large-scale magnetic fields between models and Earth automatically implies that large-scale simulated flows are realistic. These flows are indeed generated by convective instabilities at large scales, a mechanism which is very different from large-scale flows being maintained by small-scale instabilities and trans-scale energy transfer in the Earth's core.

The recent emergence of an inverse problem framework for numerical dynamos (Aubert & Fournier 2011; Fournier *et al.* 2011) and the excellent match of selected models to the geomagnetic field prompted the idea to use velocity statistics from Earth-like numerical dynamos as a statistical prior in the underdetermined inversion for flow throughout the core. This forms goal (1) of the present work. Subsequent goals are: (2) investigate the general ability of numerically simulated flows to quantitatively account for the geomagnetic secular variation, (3) handle the underdetermination of the geomagnetic inverse problem in order to produce flow images in the entire volume of Earth's core, (4) assess the robustness of quasi-geostrophic flow images against this new approach, (5) highlight the parts of the flow signal requiring additional modelling and finally (6) pave the way for time-dependent, prospective geomagnetic data assimilation algorithms.

In an initial approach of the subject (Aubert & Fournier 2011; Fournier *et al.* 2011), we have shown that good recovery of the internal structure of numerical dynamos could be achieved by applying the theory of linear estimation in weakly non-linear cases. In the generally non-linear context of the core flow problem, the linear estimation has a limited applicability and works only if we solve for small increments, starting from initial guesses not too far from the final solution. Although such a situation is expected to happen routinely in a properly implemented data assimilation algorithm (Fournier *et al.* 2010), the application is difficult for a single-epoch inversion, or for the first inversion of a data assimilation sequence, since our best initial guesses are the time average fields of the dynamo simulation and the increments are expected to be as large as these guesses (see for instance fig. 3 in Fournier *et al.* 2011). Here, the approach is thus modified to resort to classical, frozen-flux linearized inversions of the core surface flow, constrained by the numerical dynamo prior statistics, before resorting to linear estimation of the deep flow. Models and methods are presented in Section 2. Section 3 presents the main results, which are discussed in Section 4.

2 MODELS AND METHODS

2.1 Numerical dynamos and geomagnetic field models

The numerical dynamo model solves for Boussinesq convection and magnetic induction in the magnetohydrodynamic approximation in a rapidly rotating spherical shell between radii r_i and r_o with the present Earth's core aspect ratio $r_i/r_o = 0.35$. A complete physical description can be found in Aubert *et al.* (2009) and Aubert & Fournier (2011). The numerical implementation PARODY-JA is used (Dormy *et al.* 1998; Aubert *et al.* 2008). Four cases have been calculated (Table 1). Models 1 and 2 originate from Aubert & Fournier (2011) and use rigid and electrically insulating boundaries. The distribution of buoyancy sources aims at mimicking chemical convection (the dominant source of buoyancy in the Earth's core at present, see Aubert *et al.* 2009). The practical implementation comprises an imposed, spatially homogeneous buoyancy flux at the inner boundary, zero buoyancy flux at the outer boundary, a sink term in the volume. Model 3 is similar to model 2, but has a stress-free outer boundary, an axially rotating, conducting inner core (with same conductivity as the outer core) subject to viscous and magnetic torques from the outer core, and to a gravitational torque from the mantle with expression $-\Gamma\tau(\Omega_{ic} - \Omega_m)$, where Ω_{ic} and Ω_m are, respectively, the inner-core and mantle rotation rate, and the coupling constant $\Gamma\tau$ is as described in Aubert & Dumberry (2011). The total (inner core, outer core and mantle) angular momentum is preserved (the mantle is also axially rotating under the influence of the opposite gravitational torque from the inner core). Model 4 is similar to model 2 but has an heterogeneous, longitudinally hemispherical imposed buoyancy flux at the inner-core boundary, in addition to the homogeneous buoyancy flux. This configuration simulates the dynamic consequences (Olson & Deguen 2012) of the inner-core translational instability (Alboussiere *et al.* 2010; Monnereau *et al.* 2010). Further details about the numerical models are reported in Table 1.

Following our previous studies (Aubert & Fournier 2011; Fournier *et al.* 2011), the non-dimensional model output is scaled back to the dimensional world using either canonical units, or units underlain by scaling principles known (or thought) to hold both in the numerical model and in the Earth's core. This is done in order to physically rationalize the parameter gap between the numerical model and the geodynamo. The canonical length unit is used, the non-dimensional shell gap $r_o - r_i$ being assigned the value 2260 km. Owing to the homogeneity of the magnetic induction equation (see Section 2.2.1), the magnetic field unit is irrelevant here and only a time unit is needed in addition to the length scale. Here the non-dimensional secular variation timescale of the model (Lhuillier *et al.* 2011) is assigned the Earth dimensional value $\tau_{SV} = 415$ yr. The ± 50 yr uncertainty range reported by Lhuillier *et al.* (2011) only has a minor effect on the flow inversion results presented in Section 3. Since the magnetic Reynolds number of models 2–4 is very close to the value of about 800 which is expected in the Earth's core (Christensen & Tilgner 2004), the choice of an advective timescale for rescaling the time axis is equivalent to the choice of a timescale based on magnetic diffusion. Finally, for the sole illustrative purpose of comparing the simulated magnetic field spectral properties to the geomagnetic field, the non-dimensional, convective-power based scaling prediction (Christensen & Aubert 2006) for the magnetic field amplitude in the models is adjusted to the dimensional value $[B] = f_{ohm}^{1/2}(\rho\mu^3 p^2 D^2)^{1/6} = 1.7$ mT predicted by a high-power present core state (Aubert *et al.* 2009). In the previous formula, p is the convective power density in the outer core and f_{ohm} the ohmic dissipation fraction of this power.

The output of the numerical models has been compared to magnetic field and secular variation spectral coefficients obtained from the geomagnetic field models CM4 (Sabaka *et al.* 2004) and gufm-sat-Q3 (Finlay *et al.* 2012). For the satellite era, this latter model is chosen because of its focus on extracting the geomagnetic signal of core origin. The magnetic field output of models 2 and 3 is morphologically fairly similar to the geomagnetic field, as attested by the low χ^2 values reported in Table 1, and as illustrated in Fig. 1. The output also includes equatorial magnetic patches of normal polarity, created by flux expulsion from radial equatorial upwellings. The patches do not have any preferential drift direction in model 2. The choice of boundary conditions in model 3 produces a sizeable equatorial zonal flow below the outer boundary (see Fig. 11 in Section 3.2.3), transporting equatorial magnetic flux patches in the westward direction at a speed comparable

Table 1. Properties of the numerical model cases. Models 1 and 2 correspond to the models fully described in Aubert & Fournier (2011). Definitions for the left panel input parameters can also be found in that study: the Rayleigh number Ra_Q, and the viscous, magnetic and thermal Ekman numbers E, E_η and E_κ. The right panel gives the values of the output parameters, as defined in the introduction: the magnetic Reynolds number Rm, the Lehnert number λ, and the measure χ^2 of morphological similarity to the geomagnetic field (Christensen *et al.* 2010). Earth values are estimated in Christensen & Aubert (2006); Aubert *et al.* (2009). Notes: (c) columnar flow, (am) angular momentum conservation (see text), with an inner core to mantle gravitational coupling constant $\Gamma\tau/\rho\nu D^3 = 5 \times 10^4$ as defined in Aubert & Dumberry (2011) (ν is the fluid viscosity), (ep) presence of equatorial magnetic flux patches of normal polarity at the outer boundary, (wdep) presence of westward-drifting equatorial flux patches of normal polarity at the outer boundary, (ich) heterogeneous buoyancy release at the inner-core boundary with peak-to-peak magnitude at 80 per cent of the homogeneous buoyancy flux, (eg) presence of an hemispherical, eccentric columnar gyre. The question marks refer to features that are conjectured, but not directly observed in the Earth's core.

	Ra_Q	E	E_η	E_κ	Rm	λ	χ^2	Notes
Model 1	5.8×10^{-4}	10^{-3}	2.5×10^{-4}	10^{-3}	100	4×10^{-2}	6	
Model 2	2.7×10^{-5}	3×10^{-5}	1.2×10^{-5}	3×10^{-5}	858	1.4×10^{-2}	1	c, ep
Model 3	2.7×10^{-5}	3×10^{-5}	1.2×10^{-5}	3×10^{-5}	982	1.3×10^{-2}	0.8	c, am, wdep
Model 4	2.7×10^{-5}	3×10^{-5}	1.2×10^{-5}	3×10^{-5}	818	1.7×10^{-2}	3	c, ich, eg
Earth	$O(10^{-13})$	3×10^{-15}	3×10^{-9}	$O(10^{-15})$	$O(10^3)$	$O(10^{-4})$		c?, eg?, wdep

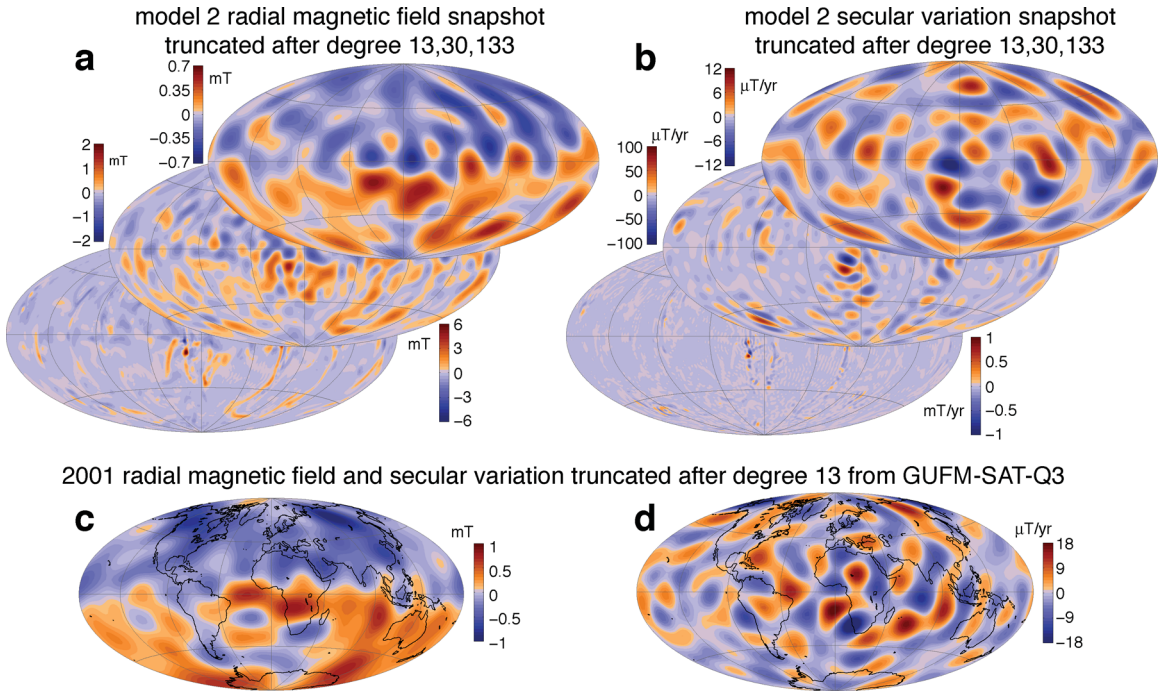

Figure 1. Core–mantle boundary radial magnetic field (a) and its rate of change (b) in a snapshot of model 2 and (c), (d) in the gufm-sat-Q3 geomagnetic field model (Finlay *et al.* 2012) for epoch 2001. Three levels of spherical harmonic truncation are presented for the model output. The geomagnetic field models are truncated at degree 13.

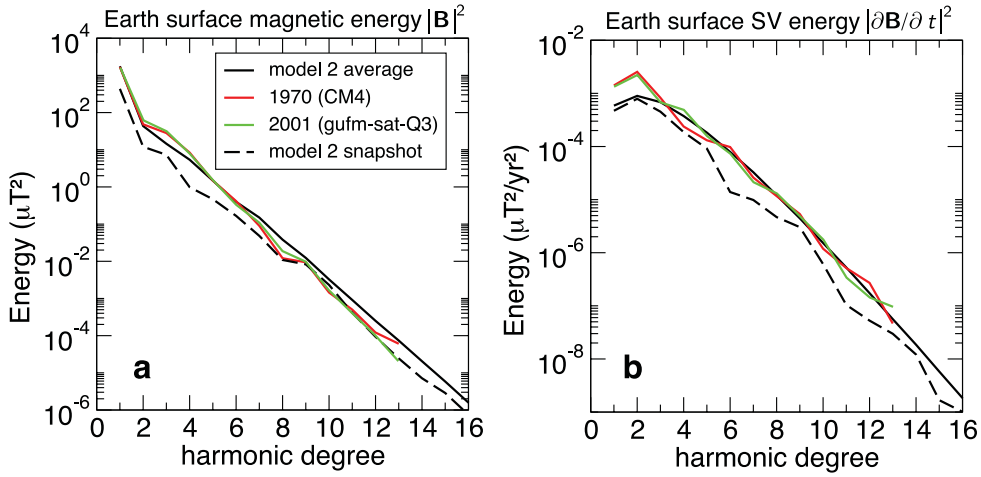

Figure 2. Energy spectra of the magnetic field (a) and its secular variation (b) at the Earth's surface, as function of the spherical harmonic degree. Two epochs of the geomagnetic field are represented (colour lines). The solid black line represents the average variance of the magnetic field and secular variation of model 2. The dashed line corresponds to the snapshot shown in Fig. 1.

to the geomagnetic westward drift. Models 2 and 3 finally appear to provide a secular variation which is very similar to the geomagnetic observations, including an important equatorial signal (with westward drift in the case of model 3). This good similarity is also attested by comparing the magnetic field and secular variation spectra of the models to the geomagnetic field (Fig. 2), although the secular variation spectra hint for model large scales ($l = 1, 2$) slightly underpowered with respect to the smaller scales when compared to the geomagnetic data. In contrast, models 1 and 4 exhibit a less Earth-like magnetic field morphology as attested by the larger χ^2 values in Table 1. Equatorial magnetic field dynamics is absent from model 1, and strongly reduced in model 4 with respect to its homogeneous counterpart model 2 (not shown). It should finally be noted that none of the simulated magnetic fields present polarity reversals. This is not considered a problem given the timescales on which the analysis is focused here.

While the velocity field in model 1 significantly deviates from columnar flow, snapshots from models 2–4 exhibit a fairly columnar behaviour (see Fig. 6 in Section 3.1), with local deviations under the influence of magnetic and thermal winds (most notably long-term polar vortices in the tangent cylinder, see also Fig. 11 in Section 3.2.3). This observation and the Lehnert number values reported in Table 1 are compatible with the condition $\lambda \leq 3 \times 10^{-2}$ proposed by Jault (2008) for the presence of columnar flow in numerical dynamos. In contrast with the other models, model 3 produces a westward zonal flow at equatorial position beneath the outer boundary (see Fig. 11). It should

finally be noted that none of the models 1–3 spontaneously generate eccentric columnar gyres, while model 4 does (see Fig. 14 in Section 3.2.4).

2.2 Inversion for core surface flows constrained by a numerical dynamo

The inversion proceeds in two stages: first, the flow below the hydromagnetic boundary layer close to the core–mantle boundary (the near-surface flow) is obtained by inverting a linearized version of the non-linear frozen-flux induction equation. The second step is a linear estimation (Aubert & Fournier 2011) of the deep flow from the near-surface flow, taking advantage of the strong linear couplings existing between the two due to the influence of the Coriolis force. This two-step formulation differs from the one-step approach undertaken in Aubert & Fournier (2011) due to the need to handle the non-linearity of the core flow problem. It should also be noted that, in contrast to the quasi-geostrophic approach, it does not necessarily involve a rigid enforcement of columnar flow at depth.

2.2.1 Surface flow

The magnetohydrodynamic induction equation is written as

$$\frac{\partial \mathbf{B}}{\partial t} = \nabla \times (\mathbf{u} \times \mathbf{B}) + \eta \nabla^2 \mathbf{B}, \tag{2}$$

where t is time, $\mathbf{B}$ the magnetic field and $\mathbf{u}$ the velocity field. It is assumed (see Finlay *et al.* 2010, for justifications) that magnetic diffusion is of secondary importance owing to the rather large magnetic Reynolds number of the core, that the radial magnetic field jump across the thin viscous Ekman boundary layer close to the core–mantle boundary is negligible, and that the radial velocity remains weak immediately outside this boundary layer. The main source for the time variation of the outer boundary radial magnetic field Br is then advection by the lateral, near-surface velocity field $\mathbf{u}_{\rm fs}$ immediately below the Ekman layer (Roberts & Scott 1965)

$$\frac{\partial Br}{\partial t} = -\nabla_H \cdot (\mathbf{u}_{\rm fs} Br) + \epsilon. \tag{3}$$

Here ∇_H is the horizontal divergence operator, and ϵ gathers all the secondary sources of secular variation which are neglected when adopting the above assumptions, and when arbitrarily truncating the spectral representations of $\mathbf{u}_{\rm fs}$ and Br as

$$Br = \sum_{\substack{-m_1^{\max} \le m \le m_1^{\max} \\ |m| \le l \le l_1^{\max}}} Br_l^m Y_l^m(\theta, \varphi), \tag{4}$$

$$\mathbf{u}_{\rm fs} = \begin{pmatrix} \dfrac{1}{\sin\theta}\dfrac{\partial T}{\partial \varphi} + \dfrac{\partial S}{\partial \theta} \\ -\dfrac{\partial T}{\partial \theta} + \dfrac{1}{\sin\theta}\dfrac{\partial S}{\partial \varphi} \end{pmatrix}, (T, S) = \sum_{\substack{-m_3^{\max} \le m \le m_3^{\max} \\ |m| \le l \le l_3^{\max}}} (t_l^m, s_l^m) Y_l^m(\theta, \varphi). \tag{5}$$

Here $l_1^{\max} = m_1^{\max} = 13$ is the degree to which the magnetic field and secular variation of core origin is assumed to be known, $l_3^{\max} = m_3^{\max} = 30$ is the degree to which core flow is expanded, $Y_l^m(\theta, \phi)$ is the complex spherical harmonic function of degree l and order m on the unit sphere mapped by the colatitude θ and the longitude φ. The lateral flow $\mathbf{u}_{\rm fs}$ is described by the toroidal and spheroidal potentials T and S. The truncation level of the flow needs to be at least twice that of the data coefficients, in order to resolve the non-linear couplings present in (3). It should however not greatly exceed that value because higher truncation levels result in increasingly costly inverse problem computations (especially at depth) and because data provided up to degree and order 13 is not expected to constrain the additional flow coefficients.

Similarly to the approach presented in Whaler (1986), the direct problem (3) then writes, for $-m_1^{\max} \le m_1 \le m_1^{\max}$, $|m_1| \le l_1 \le l_1^{\max}$:

$$\frac{\partial Br_{l_1}^{m_1}}{\partial t} = -\frac{1}{r_{\rm o}} \sum_{\substack{-m_1^{\max} \le m_2 \le m_1^{\max} \\ |m_2| \le l_2 \le l_1^{\max}}} Br_{l_2}^{m_2} \sum_{\substack{-m_3^{\max} \le m_3 \le m_3^{\max} \\ |m_3| \le l_3 \le l_3^{\max}}} \left(E_{l_1,l_2,l_3}^{-m_1,m_2,m_3} \cdot t_{l_3}^{m_3} + AG_{l_1,l_2,l_3}^{-m_1,m_2,m_3} \cdot s_{l_3}^{m_3} \right) + \epsilon_{l_1}^{m_1}, \tag{6}$$

where $r_{\rm o}$ is the core–mantle boundary radius,

$$A = \frac{1}{2}\left[l_2(l_2+1) - l_1(l_1+1) - l_3(l_3+1) \right], \tag{7}$$

$\epsilon_{l_1}^{m_1}$ is the spherical harmonic expansion of the error ϵ, and E, G are the Elsasser and Adams–Gaunt integrals

$$E_{l_1,l_2,l_3}^{m_1,m_2,m_3} = \int_{\mathcal{S}} Y_{l_1}^{m_1} \left(\frac{\partial Y_{l_2}^{m_2}}{\partial \theta}\frac{\partial Y_{l_3}^{m_3}}{\partial \varphi} - \frac{\partial Y_{l_3}^{m_3}}{\partial \theta}\frac{\partial Y_{l_2}^{m_2}}{\partial \varphi} \right) \mathrm{d}\theta \mathrm{d}\varphi, \tag{8}$$

$$G^{m_1,m_2,m_3}_{l_1,l_2,l_3} = \int_{\mathcal{S}} Y^{m_1}_{l_1} Y^{m_2}_{l_2} Y^{m_3}_{l_3} \sin\theta \, \mathrm{d}\theta \mathrm{d}\varphi. \tag{9}$$

These integrals relate to Wigner coefficients (James 1973) and are non-zero only for particular combinations of $l_{1,2,3}$, $m_{1,2,3}$ respecting triangular rules. They can be numerically evaluated in an efficient manner (here the algorithms and fortran routines detailed in Moon 1979, are used). The direct problem (6) is non-linear, and linearized for each single epoch as

$$\mathbf{y} = \mathbf{M}(Br_l^m)\mathbf{x}_{\mathrm{fs}} + \epsilon. \tag{10}$$

Here $\mathbf{y}$ is the data vector containing the 196 complex coefficients $\partial Br_l^m/\partial t$, $-m_1^{\max} \leq m \leq m_1^{\max}$, $|m| \leq l \leq l_1^{\max}$. These reduce to $N_d = 195$ real degrees of freedom, accounting for the facts that Br_l^{-m} and Br_l^m are complex conjugates and that $Br_0^0 = 0$. The vector $\mathbf{x}_{\mathrm{fs}}$ is the state vector containing the 1922 complex near-surface flow coefficients t_l^m, s_l^m, $-m_3^{\max} \leq m \leq m_3^{\max}$, $|m| \leq l \leq l_3^{\max}$. Here again these reduce to $N_{\mathrm{m}} = 1920$ real degrees of freedom. The matrix $\mathbf{M}$ contains the magnetic field coefficients and coupling integrals. The inversion of Eq. (10) usually implies additional assumptions to handle the underdetermination of this problem (since the number of unknowns N_{m} is larger than the number of equations N_d), as well as regularizations to ensure that the solution is well-behaved from various point of views (see Finlay *et al.* 2010, for a review). In the present approach, the statistics provided by the numerical dynamo model handle both the underdetermination and regularization of the inversion, and provide a unique solution, clearly connected to the first-principle physical content of the numerical dynamo. This situation is arguably preferable to the use of weak regularization norms involving adjustable damping parameters used in quasi-geostrophic core flow inversions (Pais & Jault 2008; Gillet *et al.* 2009). Furthermore, the misfit norm associated to the statistical prior can also be used to detect flow components which are compliant with or deviating from the prior assumptions. To these ends, the state vector $\mathbf{x}_{\mathrm{fs}}$ is centered by removing a time average value $\overline{\mathbf{x}}_{\mathrm{fs}}$ obtained from the numerical dynamo, such that $\mathbf{x}_{\mathrm{fs}} = \overline{\mathbf{x}}_{\mathrm{fs}} + \tilde{\mathbf{x}}_{\mathrm{fs}}$. We then solve the problem

$$\mathbf{M}\tilde{\mathbf{x}}_{\mathrm{fs}} = \mathbf{y} - \mathbf{M}\overline{\mathbf{x}}_{\mathrm{fs}} - \epsilon. \tag{11}$$

Introducing the statistical covariance matrix $\mathbf{P}_{\mathrm{fs}}$ for the components of the near-surface flow $\tilde{\mathbf{x}}_{\mathrm{fs}}$, and the error covariance matrix $\mathbf{R}$ for the components of the error $\boldsymbol{\epsilon}$, the stochastic inverse is (Aubert & Fournier 2011)

$$\tilde{\mathbf{x}}_{\mathrm{fs}} = \mathbf{K}_{\mathrm{fs}} \left(\mathbf{y} - \mathbf{M}\overline{\mathbf{x}}_{\mathrm{fs}} \right), \tag{12}$$

with the Kalman gain matrix

$$\mathbf{K}_{\mathrm{fs}} = \mathbf{P}_{\mathrm{fs}}\mathbf{M}' \left(\mathbf{M}\mathbf{P}_{\mathrm{fs}}\mathbf{M}' + \mathbf{R} \right)^{-1}. \tag{13}$$

Here the prime denotes the transpose complex conjugate. Similarly as in Fournier *et al.* (2011) and Aubert & Fournier (2011), the time average state vector $\overline{\mathbf{x}}_{\mathrm{fs}}$ and near-surface flow covariance matrix $\mathbf{P}_{\mathrm{fs}}$ are directly computed from a free run of the numerical dynamo model, by stacking about 1000 decorrelated model snapshots and obtaining the first and second statistical moments. In Aubert & Fournier (2011), it was shown that the minimal temporal spacing between snapshots for obtaining a satisfactory decorrelation was the e-folding time τ_e of the system. For the priors computed here, the temporal spacing was set to $3\tau_e$. The computation of $\mathbf{P}_{\mathrm{fs}}$ is performed up to spherical harmonic degree and order 30, accordingly with the truncation level of the near-surface flow. The radius of the base of the hydromagnetic boundary layer is set at 200 km below the outer boundary in case 1, 80 km below the outer boundary in cases 2 and 4, and at the outer boundary in case 3 (since this boundary is stress free). The structure of $\mathbf{P}_{\mathrm{fs}}$ is presented in Fig. 3. The block-diagonal structure is reminiscent of the results presented in Aubert & Fournier (2011) and highlights the leading influence of the Coriolis force, which linearly couples adjacent harmonic degrees l within a block of constant harmonic order m, but does not couple distinct harmonic orders. Significant linear couplings also exist between the spheroidal and toroidal components of the flow, reflecting the tight connection between surface flow rotation and upwelling usually observed in numerical dynamos (see e.g. Aubert *et al.* 2008).

The error covariance matrix $\mathbf{R}$ is iteratively determined, following a procedure reminiscent from Pais & Jault (2008). The initial error covariance matrix is assumed to be made up by a constant times the identity matrix. Then an initial velocity field $\mathbf{v}$ is obtained, from which the underparametrization error, or secular variation resulting from the influence of the velocity field with the unresolved magnetic field, is computed and added to the error arising from the neglect of magnetic diffusion and the observation error (these three sources are supposed to be statistically independent and to overcome all the other sources)

$$\left|\epsilon_l^m\right|^2 = \left|\left[\nabla_H \cdot (\mathbf{v}Br_{13<l\leq 30})\right]_l^m\right|^2 + \left|\left[\eta \mathbf{e}_r \cdot \Delta\mathbf{B}\right]_l^m\right|^2 + \epsilon_0(l)^2. \tag{14}$$

Here $Br_{13<l\leq 30}$ is the small-scale part of the radial field at the core-mantle boundary between degrees 14 and 30 (the contribution from higher degrees has been checked to be negligible in all numerical dynamo models presented here), and $\eta \mathbf{e}_r \cdot \boldsymbol{\Delta}\mathbf{B}$ is the radial part of near-surface magnetic diffusion. Both quantities are linearly estimated from the known part of the core–mantle boundary magnetic field and secular variation, and the prior numerical model covariance properties, following the procedure outlined in Fournier *et al.* (2011) and Aubert & Fournier (2011). Fig. 4 presents examples of such linear estimations. The data noise background $\epsilon_0(l)^2$ is set to correspond, at the Earth surface, to a flat energy spectrum per degree, at a level of 0.02 $(\mathrm{nT\,yr^{-1}})^2$ for gufm-sat-Q3 (Pais & Jault 2008) and 0.4 $(\mathrm{nT\,yr^{-1}})^2$ for CM4 (Gillet *et al.* 2009). From this single realization of the error ϵ_l^m, an l-dependent statistical error model is constructed as

$$f(l) = \frac{1}{l+1} \sum_{m=0}^{l} |\epsilon_l^m|^2/(\sigma_{lm})^2, \tag{15}$$

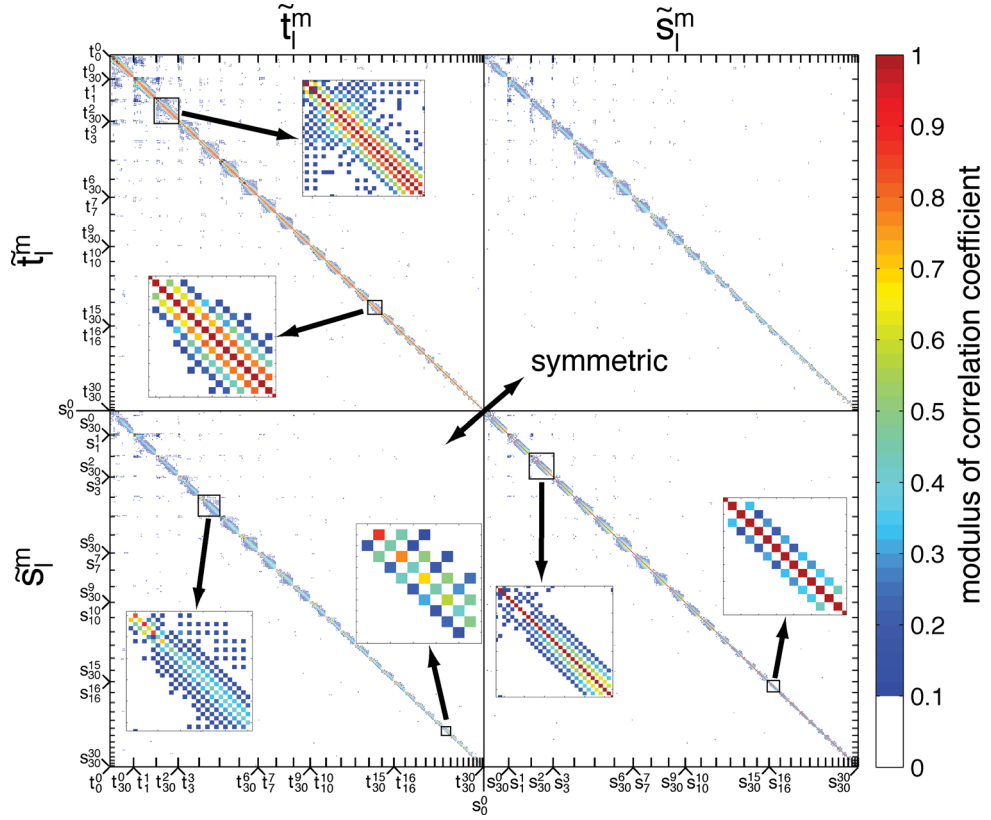

Figure 3. Variance-normalized modulus of the covariance matrix $\mathbf{P}_{\rm fs}$ for the statistically centered toroidal and spheroidal components $\tilde{t}_l^m$ and $\tilde{s}_l^m$ of the near-surface flow in model 2. Close-ups of selected regions are also enlarged.

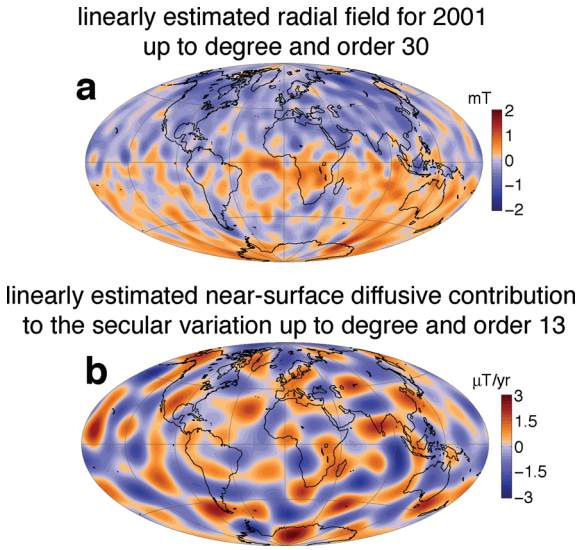

Figure 4. (a) Radial magnetic field at the core-mantle boundary in 2001 up to harmonic degree and order 30, linearly estimated from gufm-sat-Q3 provided up to degree and order 13 and from the magnetic field statistics of model 2, following the procedure outlined in Fournier *et al.* (2011); Aubert & Fournier (2011). (b) Near-surface radial magnetic diffusion up to degree and order 13, linearly estimated from the same data and magnetic field statistics as in (a).

where σ_{lm} is the prior model variance for individual secular variation coefficients (This quantity is computed during the free dynamo model run simultaneously with the flow statistics). The matrix $\mathbf{R}$ is finally updated as a diagonal matrix following this error model

$$R_{l'l}^{mm} = (\sigma_{lm})^2 f(l). \tag{16}$$

The scheme is iterated until convergence (typically 10 iterations). The data fit quality is measured through the normalized data misfit

$$\Delta_d = \frac{1}{N_d}\sqrt{(\mathbf{y} - \mathbf{M}\mathbf{x}_{\rm fs})' \mathbf{R}^{-1} (\mathbf{y} - \mathbf{M}\mathbf{x}_{\rm fs})}. \tag{17}$$

The energy of the inverse solution with respect to the statistical prior is evaluated through the normalized deviation to the prior model time average

$$\Delta_{\rm m} = \frac{1}{N_{\rm m}} \sqrt{\tilde{\mathbf{x}}'_{\rm fs} \mathbf{P}_{\rm fs}^{-1} \tilde{\mathbf{x}}_{\rm fs}}. \tag{18}$$

In the process of searching for the most probable solution given the data and the model statistics, the inversion (13) minimizes the functional (Aubert & Fournier 2011)

$$\mathcal{J}(\mathbf{x}) = (\mathbf{y} - \mathbf{M}\mathbf{x}_{\rm fs})' \, \mathbf{R}^{-1} \, (\mathbf{y} - \mathbf{M}\mathbf{x}_{\rm fs}) + \tilde{\mathbf{x}}'_{\rm fs} \mathbf{P}_{\rm fs}^{-1} \tilde{\mathbf{x}}_{\rm fs}. \tag{19}$$

The inversion approximately balances each individual harmonic coefficient contribution in $\mathcal{J}$. It is thus expected that for a correct fit to the data ($\Delta_d \approx 1$), the deviation from the prior model time average will be $\Delta_{\rm m} \approx \sqrt{N_d / N_{\rm m}} \Delta_d < 1$ since the spherical harmonic expansion of the model exceeds that of the data by about a factor 10.

2.2.2 Deep flow

Once a near-surface flow inverse is obtained, a linear estimation of the corresponding deep flow is performed. The 3-D velocity vector

$$\tilde{\mathbf{x}} = \left[\tilde{t}_l^m(r_{\rm i}), \ldots, \tilde{t}_l^m(r_{\rm o}), \tilde{s}_l^m(r_{\rm i}), \ldots, \tilde{s}_l^m(r_{\rm o}) \right]^T, \tag{20}$$

where superscript T denotes the transpose, gathers the values of the statistically centred toroidal and spheroidal potentials of the velocity field $\mathbf{u}$ on the nodes of a numerical discrete grid (82 radial levels are used). The direct problem is written

$$\mathbf{H}\tilde{\mathbf{x}} = \tilde{\mathbf{x}}_{\rm fs}, \tag{21}$$

or, in an expanded form

$$\begin{pmatrix} 0 & \ldots & 0 & 1 & 0 & \ldots & \ldots & \ldots & \ldots & 0 \\ 0 & \ldots & \ldots & \ldots & \ldots & 0 & 1 & 0 & \ldots & 0 \end{pmatrix} \begin{pmatrix} \tilde{t}_{lm}(r_{\rm i}) \\ \vdots \\ \tilde{t}_{lm}(r_E) \\ \vdots \\ \tilde{t}_{lm}(r_o) \\ \tilde{s}_{lm}(r_{\rm i}) \\ \vdots \\ \tilde{s}_{lm}(r_E) \\ \vdots \\ \tilde{s}_{lm}(r_o) \end{pmatrix} = \begin{pmatrix} \tilde{t}_{lm}(r_E) \\ \tilde{s}_{lm}(r_E) \end{pmatrix}. \tag{22}$$

Here r_E is the radius of the base of the hydromagnetic boundary layer and $\mathbf{H}$ is called the observation operator, containing ones in the cells where the quantity is observed, and zeros otherwise. This vastly underdetermined problem is again solved under constraint of a numerical dynamo prior model covariance matrix $\mathbf{P}$ cross-correlating all flow components (Aubert & Fournier 2011)

$$\tilde{\mathbf{x}} = \mathbf{K}\tilde{\mathbf{x}}_{\rm fs}, \tag{23}$$

with the Kalman gain matrix

$$\mathbf{K} = \mathbf{P}\mathbf{H}' \left(\mathbf{H}\mathbf{P}\mathbf{H}' \right)^{-1}. \tag{24}$$

The matrix $\mathbf{P}$ is computed using the same procedure as for $\mathbf{P}_{\rm fs}$ (which is a subset of $\mathbf{P}$), and to the same spectral resolution. Its structure is quite similar to the structures already described in detail in Fig. 3 of this study and fig. 3 of Aubert & Fournier (2011), block-diagonal with non-existent couplings between different m-values but significant couplings between adjacent l-values within an m-block, and also exhibits couplings between spheroidal and toroidal terms. Once the spheroidal and toroidal potentials are determined throughout the shell, the velocity field $\mathbf{u}$ can easily be determined after computing the poloidal potential $p_{lm}(r)$ through $s_{lm}(r) = \partial [r p_{lm}(r)] / r \partial r$.

3 RESULTS

3.1 Validation with synthetic experiments

In order to estimate the efficiency of the whole core flow inversion procedure, we first invert synthetic secular variation data, extracted and realistically truncated from the model 2 snapshot presented in Fig. 1, and compare the recovered flow with the known reference velocity field of this snapshot. Table 2 summarizes the experiments performed. The recovery quality is quantitatively evaluated using the correlation

Table 2. Description of synthetic experiments and diagnostics for recovery quality. Correlation coefficients and pointwise recovery factors are defined as in Amit *et al.* (2007), and evaluated between the recovery and reference truncated up to degree 30 (first number) and 13 (second number).

Exp.	Correlation coefficient	Pointwise recovery factor	Δ_d	Δ_m	Notes
1	0.51, 0.70	0.4, 0.56	1.10	0.44	Twin experiment, actual small-scale *Br* and magnetic diffusion are used for error computation
2	0.50, 0.69	0.4, 0.56	1.27	0.57	Same as (1), with linearly estimated errors, relevant situation for the geomagnetic case
3	0.32, 0.38	0.25, 0.32	1.29	0.57	Same as (2), fraternal experiment using statistical prior from model 1

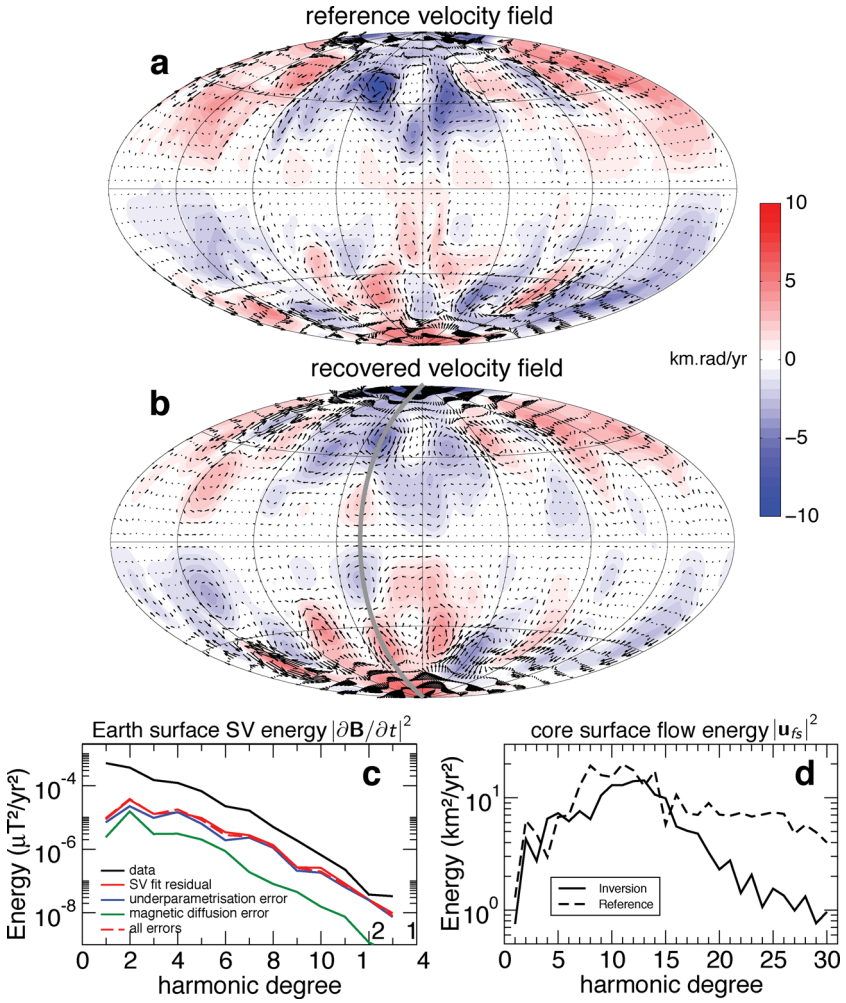

Figure 5. Core surface flow recovery versus the reference for experiment 2. (a) Hammer projection of the near-surface reference flow (arrows, arbitrary scaling) superimposed with a colour map of the near-surface toroidal scalar T (blue denotes a clockwise circulation when seen from the North pole). (b) same as (a), for the recovered near-surface flow. The grey meridian locates the meridional cut drawn in Fig. 6. (c) Earth-surface energy spectrum of the secular variation (black) as a function of the spherical harmonic degree. The residual left by the inversion (red), matches the sum (dashed red) of the modelled sources of error (blue and green). (d) Energy spectrum of the near-surface reference and recovered flows, as functions of the spherical harmonic degree.

coefficient between the reference and the recovered flows, and the pointwise recovery factor already introduced in earlier similar tests (full definitions in Amit *et al.* 2007). The synthetic data is considered noise-free, but subject to the already introduced underparametrization and magnetic diffusion errors.

Experiments 1 and 2 are twin experiments, as they use as statistical prior the same model that served to produce the synthetic data (but the snapshot under consideration is not part of the ensemble that produced the covariance matrices). Experiment 1 assumes perfect knowledge of the small-scale magnetic field and near-surface magnetic diffusion, while experiment 2 performs a linear estimation of these hidden quantities from the known quantities (this is the realistic case). The near-surface flow recovery quality is fair in both cases (Table 2 and Fig. 5), especially at larger scales. The truncated geomagnetic data indeed do not constrain well the flow at harmonic degree larger than 15 (Fig. 5d). Data misfits are close to 1, as expected from twin experiments, where data and model are compatible by construction. Deviations

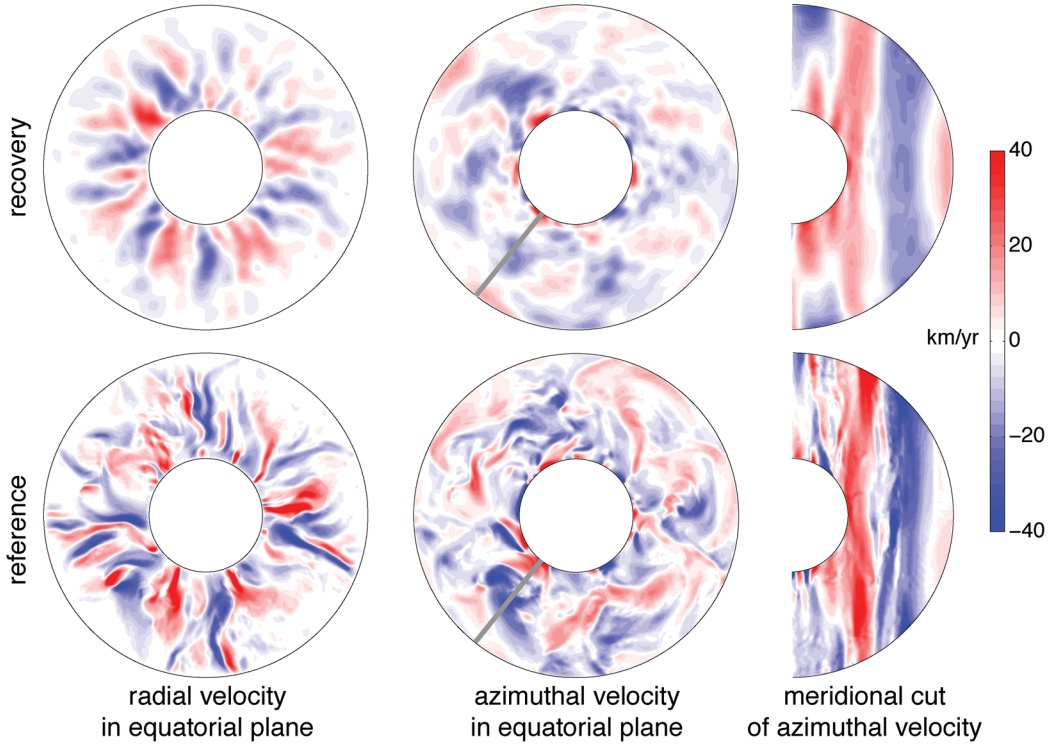

Figure 6. Deep flow recovery from the near-surface flow obtained in experiment 2, plotted against the reference flow. The grey lines locate the azimuth of the meridional cut (same position also located in Fig. 5).

to the prior model time average are on the order of 0.5, consistently with Fig. 5(d) and $N_\mathrm{m} > N_d$. The use of linearly estimated near-surface magnetic diffusion and small-scale magnetic fields (as in Fig. 4) instead of the actual quantities does not lower the recovery quality, but results in slightly larger data misfits. Experiment 3 is a fraternal experiment using a different statistical prior (here model 1) instead of the model that served to produce the synthetic data. This represents a situation where the prior presents an oversimplified description of the physics underlying the data. The inversion yields almost the same data misfit, a result which is surprising owing to the very distinct magnetic field morphologies of models 1 and 2 (see fig. 3 in Fournier *et al.* 2011, and Fig. 1 a). The recovery quality is degraded, but again surprisingly good considering that the velocity field of model 1 (again fig. 3 in Fournier *et al.* 2011) is morphologically very distinct from (and simpler than) that of model 2. The recovery quality in experiment 3 is in line with the results of Rau *et al.* (2000), Amit *et al.* (2007), while experiment 2 generally yields better results, owing to the benefits of error handling and appropriate prior statistical knowledge.

The quality of the deep flow recovery is evaluated in Fig. 6 from the surface results of experiment 2. Here the disparity between the numbers of model and data degrees of freedom is acting twice (once at the stage of near-surface flow inversion, once at the stage of deep flow inversion). The combination of the two effects attenuates the peak-to-peak magnitude of the recovery by about a factor two with respect to the reference, while still maintaining the correct amplitude for the larger flow scales (the behaviour is qualitatively similar to that observed in Fig. 5d). The most energetic features of the reference are well rendered in a morphological sense. However, there are obviously a number of small-scale details missing in the recovery, which can thus be reasonably trustworthy if the focus is set on the large-scale, most energetic features.

3.2 Geomagnetic inversions

Single-epoch inversions are performed using the geomagnetic data from models CM4 (in 1970, 1975, 1980, 1990, 1995, 2000) and gufm-sat-Q3 (in 2000, 2001, 2002.5, 2004, 2010). It is emphasized that the present inversion scheme does not regularize the solutions in time. Table 3 reports the quantities Δ_d and Δ_m for both geomagnetic field models. With respect to the results obtained in the previous synthetic

Table 3. Normalized misfit to the data Δ_d, and normalized deviation to the model time average Δ_m obtained when inverting the two geomagnetic field models with the four priors described in Section 2.1. The values reported are averages over the six epochs investigated in CM4, and the five epochs investigated in gufm-sat-Q3.

Δ_d with prior	1	2	3	4	Δ_m with prior	1	2	3	4
CM4	0.88	1.12	0.89	0.94	CM4	0.45	0.54	0.49	0.5
gufm-sat-Q3	1.34	1.32	1.18	1.22	gufm-sat-Q3	0.54	0.52	0.46	0.53

inversion experiments (Table 2), all inversions provide acceptable fits to the data, and the deviations of all inverted velocity fields from the prior models time average are standard. The difference in the level of data misfit Δ_d between CM4 and gufm-sat-Q3 originates in the different values attributed to the noise background (see Section 2.2.1). In that respect, the noise background chosen for CM4 seems appropriate (Δ_d close to 1) while it is slightly optimistic for gufm-sat-Q3 (as was already mentioned in Pais & Jault 2008). In that latter case, the data misfit remains nevertheless reasonable as it is comparable to that obtained in synthetic experiments 2 and 3. As we shall see in the following, prior models 3 and 4 have been elaborated to physically resolve deviations observed in inversions with prior 2, and yield consistently better (closer to one) data misfits with both geomagnetic field models. Prior model 1 yields data misfits comparable to prior model 2.

In the following, inversions performed with prior model 2 are first investigated in detail. Model 2 is the central model to this study as it is the most generic in terms of dynamo modelling [the model was part of a systematic parametric study in Christensen *et al.* (2010) and investigated in Aubert & Fournier (2011)]. Model 1 is also generic but less physically realistic. Its purpose is an assessment of the general robustness of the inversion. Inversions performed with models 3 and 4 are then investigated in order to attempt to explain and resolve the deviations observed with model 2.

3.2.1 Inversions with prior model 2

The near-surface flow inversion for 2001 (Fig. 7a) recovers most previously obtained core surface flow features (Finlay *et al.* 2010), such as a counter-clockwise gyre under the southern tip of Africa, a clockwise gyre east of Quebec, a westward equatorial flow under the Atlantic ocean. The numerical dynamo prior imposes a high level of equator symmetry outside the axial cylinder tangent to the inner core, and each gyre gains a symmetric counterpart (although the flow is not perfectly equator-symmetric as in quasi-geostrophic inversions). The flow also presents a markedly hemispherical longitudinal pattern, with opposite rotations in the Atlantic and Pacific hemispheres. Deeper in the core (Figs 7b and c), the highly equator-symmetric near-surface flow connects to a columnar flow (Fig. 7b), where five large-scale convective cells can be identified. Maps of the deep azimuthal velocity (Fig. 7c) also reveal a pair of nested columnar spirals anchored at the inner-core boundary, inheriting their hemispherical character from the near-surface circulation. Together with the cylindrical radial flow (equatorial map in Fig. 7b), they define a planetary-scale circulation where upwelling from the eastern part of the inner-core boundary turns into eastward flow as it moves upwards, and westward flow turns into downwelling in the Western Hemisphere as it approaches the inner-core boundary. The westward (blue) part of this structure is stronger than its eastward counterpart and coincides with the quasi-geostrophic eccentric equatorial gyre (Pais & Jault 2008), but touches the inner-core boundary instead of closing on itself. Similar images are found throughout the period 1970–2010 (Fig. 8), showing that the robustness and persistence of the gyre is supported by the present inverse geodynamo modelling approach. It should be noted that quasi-geostrophic columnar motion outside the tangent cylinder is thus robustly obtained without being explicitly enforced. Here it arises as a consequence of the physics contained in the prior. At the same time, the prior physics also permits ageostrophic deviations such as thermal-wind driven polar vortices in the tangent cylinder (rotating westwards close to the core–mantle boundary and eastwards close to the inner-core boundary).

Fig. 9(a) shows that the inverted flow satisfies the data within the specified error level, as the residual left by the inversion (solid red) is comparable to the sum (dashed red) of the modelled sources of error (the underparametrization error, blue, the magnetic diffusion error, green, and the noise background, black). The near-surface flow is also generally compliant with the prior (Fig. 9b), as most individual flow components remain within the 2σ variance level when normalized with respect to the corresponding free run variance. This shows that Earth-like, homogeneous numerical dynamos can provide a statistically compelling explanation of the geomagnetic secular variation. In the present case however, only three spectral coefficients of the solution, t_1^0, t_3^0 and t_2^1, have variances exceeding the natural variability of the prior by more than a factor 2. This underlines two important weaknesses of prior model 2, to which the inversion responds by stretching the solution beyond the admissible statistical bounds provided by the prior. The two zonal coefficients t_1^0 and t_3^0 relate to the inability of the prior to provide enough azimuthally averaged westward drift, while the coefficient t_2^1 relates to inability to produce a sizeable hemispherical flow difference between the Atlantic and Pacific hemispheres (see insets in Fig. 9b).

3.2.2 Inversions with prior model 1 and robustness to a change of prior

Fig. 10 presents the near-surface inversion result for the same data as in Fig. 7, but now using prior model 1. Flows inverted using prior models 1 and 2 are broadly similar at the largest (hemispherical) scales. Features well-identified in the literature such as the Quebec and southern Atlantic vortices are consistently reproduced by both inversions. In contrast, the two inversions are markedly different at some other locations (such as under India). Prior model 1 is less columnar than model 2, and this feature is also seen in the inversion result (compare the magnitude of the northern and southern Pacific vortices). Flow inverted using prior model 1 is also slightly less energetic. Similarly to what was observed with model 2, the inversion performed with model 1 needs to stretch the statistical deviation of the zonal and hemispherical flow coefficients previously identified (not shown). The flow inversion result presented in Fig. 10 can be directly compared to the flow model in fig. 9 of Fournier *et al.* (2011), as it uses the same inversion prior and similar geomagnetic data. The two flows are morphologically very different, highlighting the limits of a purely linear estimation of core surface flow from geomagnetic data, as discussed in Section 1. In addition to rendering a pattern which is significantly more compatible with the previous literature on core flow inversions, the present inversion also renders a stronger flow (maximum 37 km yr^{-1} versus 22 km yr^{-1} in Fournier *et al.* 2011). The scheme indeed requests the

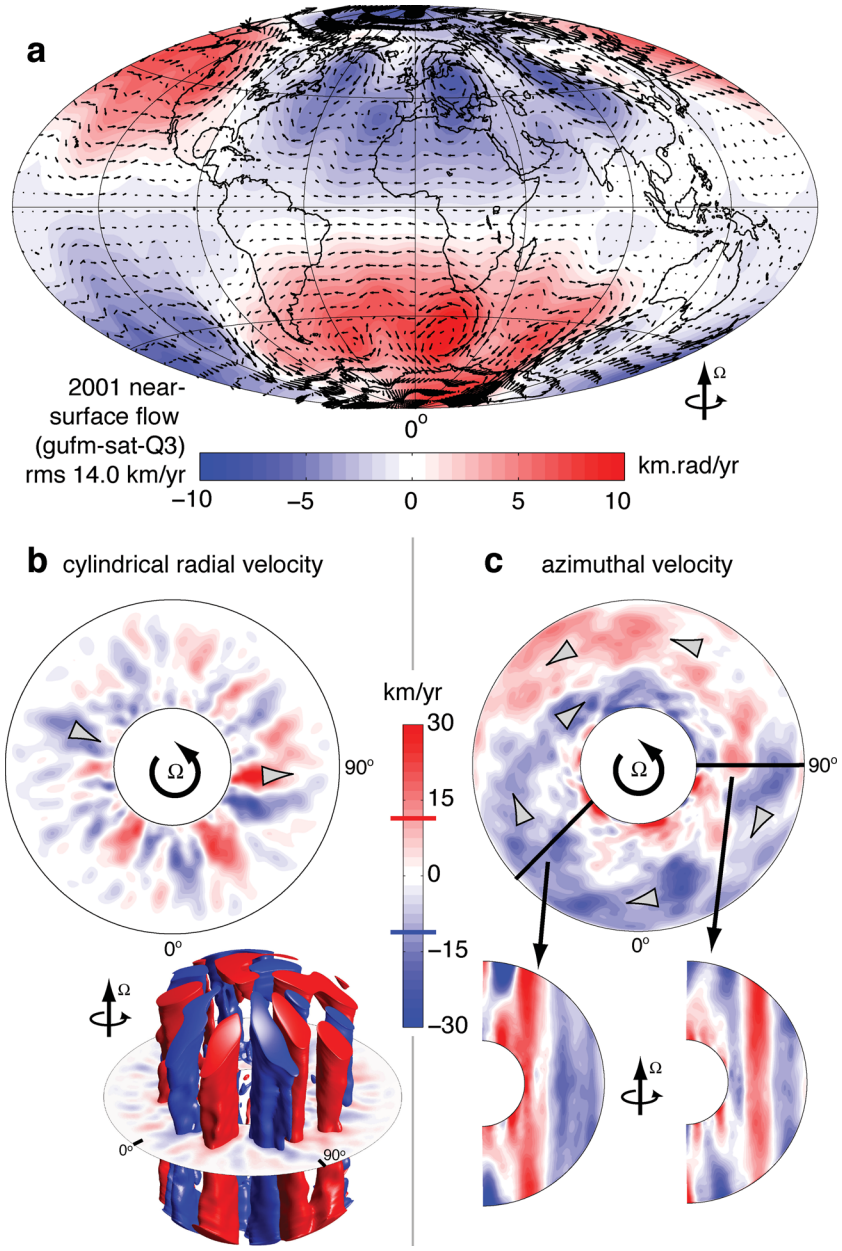

Figure 7. Flow throughout the Earth's core in 2001 from gufm-sat-Q3, inverted using prior model 2. (a) Atlantic-centered Hammer projection of the near-surface flow (arrows, arbitrary scaling) superimposed with a colour map of the near-surface toroidal scalar T (blue denotes a clockwise circulation when seen from the North pole). (b) Equatorial map (top) and isosurfaces (bottom) of the cylindrical radial velocity (red denotes an outward flow). The isosurface levels are marked on the colour bar. (c) Equatorial map (top) and meridional cuts (bottom) of the azimuthal flow. Grey arrows in (b), (c) indicate the general flow circulation. In (c), the westward eccentric columnar gyre appears in blue.

frozen-flux equation to be satisfied, thus setting an amplitude requirement on the flow. Such a requirement is not present in a linear estimation of the flow based solely on its statistical correlations with magnetic field and secular variation data, as done in Fournier *et al.* (2011).

3.2.3 Prior model 3, resolution of the t_1^0–t_3^0 deviation, and l.o.d. variations

The difficulties encountered with the t_1^0–t_3^0 pair in Fig. 9(b) are indicative of a general inability of standard numerical dynamos to render a westward-drifting zonal flow below the outer boundary at equatorial position. It has been suggested that an heterogeneous mantle control could partially resolve this problem (Olson & Christensen 2002). Here an alternative approach is taken, attempting to explain westward drift within the context of an homogeneous dynamo mechanism. The zonal flow configuration in numerical dynamos with rigid boundaries is robust to parameter variations, with shear created across the shell by the combined influence of buoyancy and magnetic forces (Aubert 2005) and resulting in an eastward flow near the inner-core boundary and almost zero rotation close to the equatorial outer boundary (Fig. 11a). It is now assumed that the outer boundary is stress free, the inner boundary free to axially rotate under the influence of viscous and magnetic torques,

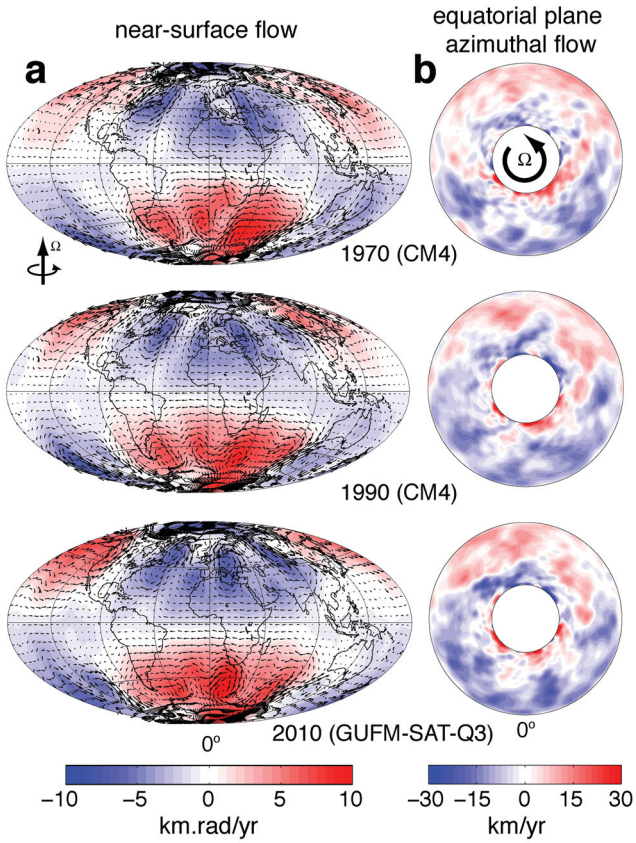

Figure 8. Near-surface flow Hammer projections (a, same conventions as Fig. 7a) and equatorial maps of the azimuthal flow (b, same convention as Fig. 7c) for epochs 1970, 1990 and 2010, using prior model 2.

that an additional gravitational torque couples the inner and outer boundaries, and that the total angular momentum of the solid core-fluid core–mantle system is preserved. Being the only torque experienced by the outer boundary in that configuration, the gravitational torque vanishes on the long term, thus maintaining alignment between the mantle and the inner core. The shear configuration then changes, with zero average fluid rotation with respect to the mantle immediately above the inner-core boundary and a sizeable westward rotation at equatorial position close to the outer boundary (Fig. 11b). A similar process operates in the simulations of Buffett & Glatzmaier (2000). Implemented in model 3, the configuration produces trains of westward-drifting equatorial magnetic flux patches of normal polarity, a feature which is very reminiscent from the behaviour of the geodynamo. It additionally provides a physically consistent mechanism for creating l.o.d. variations. Geomagnetic inversions performed with prior model 3 (Fig. 12a) shift the near-surface flow configuration observed in Fig. 7 towards a state where the westward zonal flow is strengthened beneath the Atlantic, and the opposite rotation previously observed in the Pacific disappears. The deep flow (Figs 12b and c) is still highly columnar, and directly reflects these near-surface changes, with a strengthened retrograde eccentric gyre and a strongly attenuated prograde gyre. The radial flow configuration remains similar, with upwelling being present mostly in the Eastern Hemisphere and downwelling in the Western Hemisphere. These images are now strikingly similar to the quasi-geostrophic inversion results (Pais & Jault 2008; Gillet *et al.* 2009). The normalized deviations of t_1^0 and t_3^0 are now inside the standard statistical deviation of the prior, with respective values of 0.98 and 0.62, down from 3.98 and 2.25 in Fig. 9(b). The decisive influence of the numerical prior for determining the zonal flow, as well as other considerations regarding the resolution of the inversion are further discussed with the study of a resolution matrix in Appendix A.

Having resolved the statistical deviation of the t_1^0–t_3^0 pair, it is interesting to compare the l.o.d. variations predicted by inversions with priors 2 and 3 throughout the period 1970–2010. The outer-core angular momentum J is computed from the inverted azimuthal flow u_φ

$$J = \rho \int_{\mathcal{V}} r \sin\theta u_\varphi \, \mathrm{d}V, \tag{25}$$

where $\mathcal{V}$ is the core volume. The core flow-induced variations in the l.o.d. then follow from the formula (Jault *et al.* 1988; Jackson *et al.* 1993)

$$\Delta\text{l.o.d.} = \frac{\Delta J}{I_c + I_\mathrm{m}} \frac{T_0^2}{2\pi}, \tag{26}$$

where Δl.o.d. is the l.o.d. variation, ΔJ is the core angular momentum variation obtained from the inversions, $I_c + I_\mathrm{m} = 8 \times 10^{37}\,\mathrm{kg\,m^{-2}}$ is the moment of inertia of the coupled core-mantle system, $T_0 = 24\,\mathrm{hr}$ is the reference l.o.d. The value used for the core density is

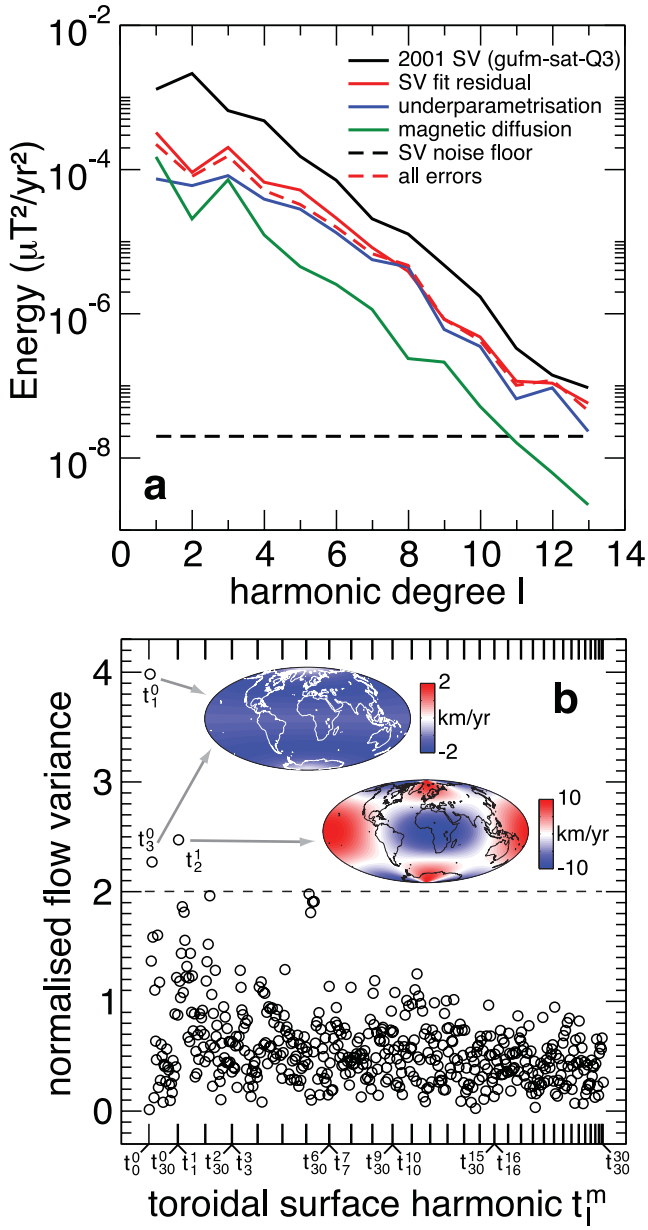

Figure 9. Fit to the geomagnetic data from gufm-sat-Q3 in 2001 using prior model 2 and deviations from the prior model. (a) Earth-surface energy spectra of the secular variation (black) as a function of the spherical harmonic degree, together with the fit quality (red), and the various modelled errors (the sum of which is represented in dashed red). (b) Variance spectrum of the individual toroidal near-surface flow spherical harmonic components. Each variance is normalized with the variance obtained from a free run of the numerical dynamo prior model. Components with variance beyond the 2σ level (dashed line) have their corresponding azimuthal flow pattern represented in the insets (blue is westwards).

$\rho = 11\,000\,\mathrm{kg\,m^{-3}}$. Fig. 13 presents the predicted and observed variations of the l.o.d. of core origin. As can be expected from the differences in zonal flow morphologies (Fig. 11), these are quite larger when using prior model 3 than with prior model 2. The ratio between the two is roughly consistent with the r.m.s. l.o.d. variations observed in free runs of the numerical priors (0.8 ms for model 2 and 3.2 ms for model 3). Both priors roughly render the long-term decrease of the l.o.d. between 1970 and 2010 (this decrease being underestimated by prior model 2 and overestimated by prior model 3). Only prior model 3 is able to correctly render the l.o.d. variations over the last 10 yr. The results obtained with prior model 3 are again very consistent with the results obtained in Gillet *et al.* (2009) with quasi-geostrophic core flow inversions.

3.2.4 Prior model 4 and resolution of the t_2^1 deviation

The statistical deviation of the t_2^1 near-surface flow coefficient displayed in Fig. 9(b) is now investigated. Here again the idea is to invoke an additional feature previously not included in standard dynamo modelling. Heterogeneous boundary control is frequently invoked to explain such planetary-scale, persistent non-zonal flow structures in the outer-core flow. The nested spirals in Fig. 7 could plausibly result from coupling with a thermally heterogeneous mantle, as the resulting flows can have a large-scale spiralling structure (Sumita & Olson 1999),

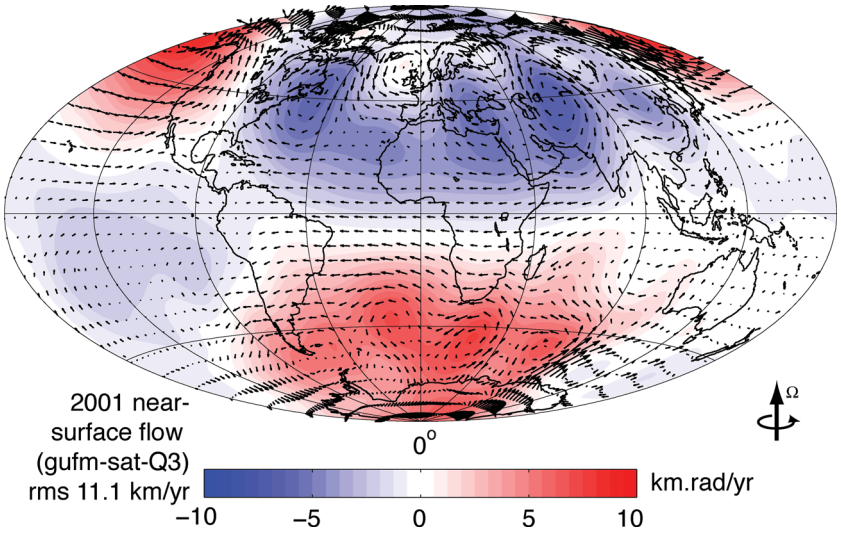

Figure 10. Near-surface core flow in 2001 from gufm-sat-Q3, inverted using prior model 1 (same conventions as Fig. 7a).

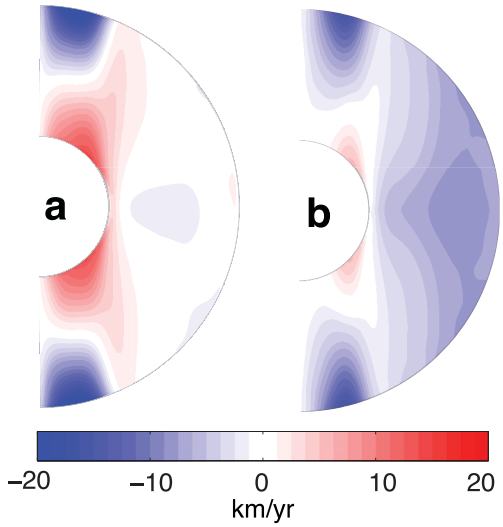

Figure 11. Meridional cuts of the time averaged and azimuthally averaged flow (blue is westwards) in free runs (unconstrained by the data) of the numerical prior models 2 (a) and 3 (b). In (b) velocities are measured with respect to the mantle.

do not drift in the mantle frame of reference, can locally account for the Atlantic westward drift (Olson & Christensen 2002) and exhibit a weak hemispherical pattern in the secular variation amplitude (Christensen & Olson 2003). However, mantle-driven flows are generally not fully longitudinally hemispherical as they inherit a harmonic order 2 structure from the seismically derived heat flow pattern imposed at the core–mantle boundary, and the orientation of their spirals tends to be mirror symmetric (Sumita & Olson 1999) to that observed here. To test the other option of a control from below, a heterogeneous buoyancy release at the inner-core boundary is added to the numerical prior model 2 to build model 4. In a first step, direct numerical simulations are performed and visually compared to the images inverted with the fully homogeneous, initial prior. A longitudinally hemispherical buoyancy pattern (Fig. 14a), with excess release below Asia yields a surface circulation, cylindrical axial (Fig. 14b) and azimuthal (Fig. 14c) deep velocity patterns strikingly similar to the images inverted with prior model 2 (Figs 7a–c). In a second step, prior model 4 is used for geomagnetic inversion, the longitudinal orientation of the hemispherical buoyancy release being varied (Fig. 14d). For epoch 2001, setting the center for excess buoyancy at about 70°E in the Asian Hemisphere yields the best variance reduction for the t_2^1 outlier (at about 0.2), while also providing a slightly better overall fit to the geomagnetic data.

4 DISCUSSION

A theoretical framework, called inverse geodynamo modelling, has been built to produce inversions of the geomagnetic secular variation for flows throughout the Earth's core, the necessary prior information being supplied by a series of numerical models of the convective geodynamo. The framework relies on classical data assimilation tools, but has been updated with respect to our previous work in order to account for the non-linearity of the core flow problem. While the approach is not perfect, as it relies on rather detailed prior information, the characteristics of which are subject to changes across the space of dynamo control parameters, it produces flows with features that are

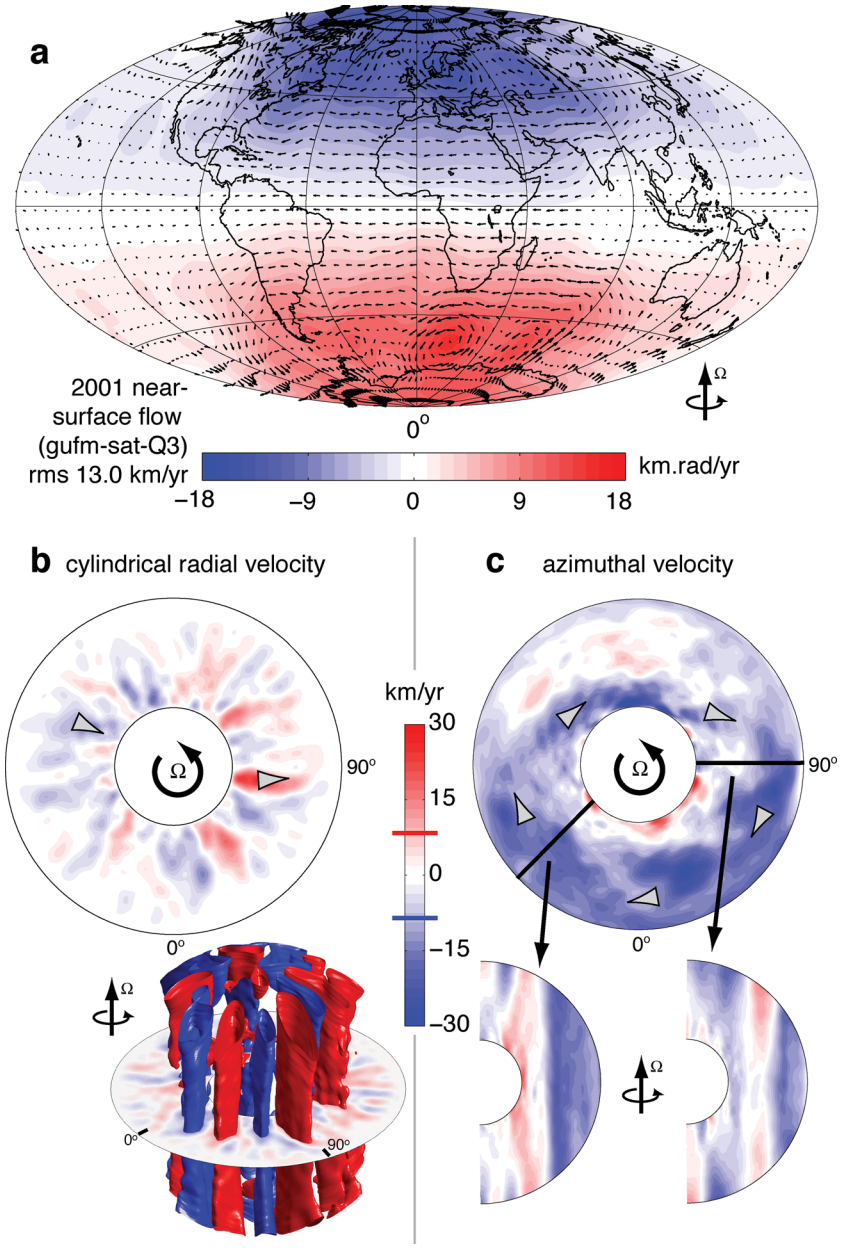

Figure 12. Flow throughout the Earth's core in 2001 from gufm-sat-Q3, inverted using prior model 3 (same conventions as in Fig. 7). In (b), the uncapped isosurfaces signal the use of a stress-free outer boundary. In (c), the strong equatorial westward zonal flow supported by the choice of boundary conditions and angular momentum conservation appears clearly.

fairly robust against changes of the prior model. This fact suggests that flows produced even by the simplest numerical dynamo fairly well describe the large-scale morphological characteristics of the much more turbulent flow generating the Earth's magnetic field, and provide a satisfactory fit to the secular variation within a realistically specified error level. The most important advantage that the method has over the classical penalized least-squares approach is probably the fact that the solution is uniquely determined (absence of damping parameters) and clearly connected to the first principle physics supplied by the numerical dynamo prior model. Observed statistical deviations can then be interpreted as shortcomings of the physical modelling. This possibility is rather novel among core flow inversion methods and has been used here to attempt to physically describe the geomagnetic westward drift, and the global longitudinal hemisphericity of the geomagnetic secular variation. Whether the proposed mechanisms are really the ones at work in the geodynamo or not is obviously still an open question, but the present work opens interesting prospects by establishing a benchmark against which modelling ideas can be quantitatively tested.

The inverted deep flow has been shown to be strongly columnar if the prior Lehnert number is small enough, the limit of $\lambda < 3 \times 10^{-2}$ proposed by Jault (2008) being compatible with the present results. Owing to the smallness of that number in the Earth case, this produces strong support to the hypothesis that flows inside Earth's core are dominantly columnar, accordingly to the quasi-geostrophic assumption. Furthermore, the results support the idea that the validity range of this assumption can be extended from short timescales (interannual to decadal) towards timescales commensurate to core overturn and diffusive processes (centennial and more), at least for flow structures outside

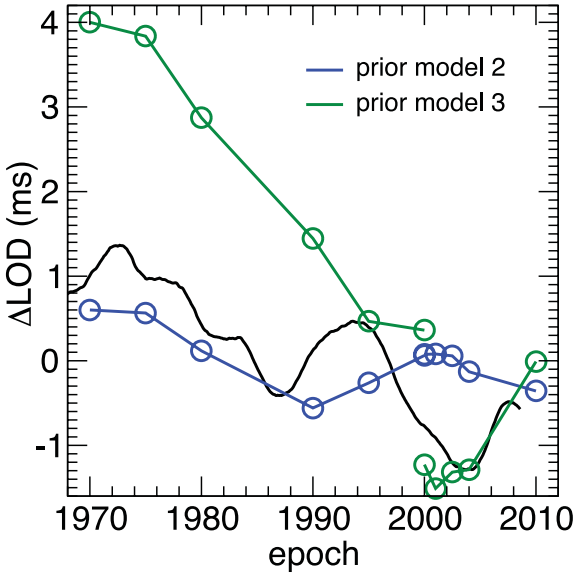

Figure 13. Predicted l.o.d variations (blue, green) versus the observed variations attributed to core flow, computed as in fig. 13 of Gillet *et al.* (2009).

the tangent cylinder. The existence of the giant eccentric westward columnar gyre proposed by Pais & Jault (2008) is thus confirmed within a framework that allows this structure to persist over centuries, as seems to be the case in the Earth. In addition to presenting features strikingly similar to quasi-geostrophic inversions, the inverted flows also have the additional strength of reconciling quasi-geostrophic, columnar flows with longer-term ageostrophic features such as polar vortices inside the tangent cylinder.

Assuming that gravitational coupling of the mantle to the inner core is indeed the mechanism producing the geomagnetic westward drift by deporting the thermal wind shear towards the vicinity of the core-mantle boundary, an additional constraint on the magnitude of gravitational coupling can be derived from Fig. 13. In order to avoid excessive variations of the l.o.d. (as produced by prior model 3 and as also seen in the results of quasi-geostrophic inversions, Gillet *et al.* 2009), a gravitational coupling constant on the order of $\Gamma\tau/\rho\nu D^3 \approx 2 \times 10^4$ should probably be used in prior model 3 (although this remains to be checked in subsequent modelling). Scaling this value back to the dimensional world using the scaling principles outlined in the introduction yields $\Gamma\tau \approx 2.3 \times 10^{20}$ N · m · yr. This is physically reasonable (Aubert & Dumberry 2011) but too small to permit the explanation of the 6-year oscillation in the l.o.d. in terms of mantle–inner-core gravitational coupling (Mound & Buffett 2006), in which case an explanation in terms of rapid Alfvén waves (Gillet *et al.* 2010) would be preferred.

Assuming that an heterogeneous buoyancy release at the inner core surface is at the origin of the hemispherical character of the secular variation and its associated velocity field structure, the giant eccentric westward columnar gyre, the present results predict that the center of the excess buoyancy release should be in the Eastern Hemisphere. The inner-core possesses an instability mode (Monnereau *et al.* 2010) causing its material to slowly translate along an axis parallel to the equatorial plane, with permanent melting in one hemisphere and crystallization in the other. The direction of translation has been inferred to be west to east based on the comparison of a variable grain size scattering model with inner-core surface seismic data. Should the light chemical elements at the origin of buoyancy be preferentially released in the crystallizing hemisphere, this would indeed induce a hemispherical longitudinal buoyancy release pattern, but with the exact opposite distribution and consequences (excess release and flow upwelling below America, deficit and downwelling below Asia) to that deduced from the present inverse geodynamo modelling results. There may be a few explanations to this discrepancy. First, the buildup of a dense layer (Alboussiere *et al.* 2010) around the inner core as a consequence of its translational instability might reconcile the two views as this layer could act as a buffer significantly distorting the buoyancy pattern. Second, it is possible that the inner-core translation direction has changed through time (Olson & Deguen 2012), in which case the results presented here would be supportive of a present translation direction opposite to the long-term trend. It should be noted that this interpretation is compatible with the location of the recent-time geomagnetic dipole eccentricity (Olson & Deguen 2012).

What should be the best numerical dynamo prior for geomagnetic inversion and data assimilation? Following the present study it is obvious that a computationally tractable case underlain by physics closest to the real system and producing the most Earth-like output should be chosen. However, it may be counterproductive to resolve all statistical deviations of a standard prior, as additional physical mechanisms need to be invoked that are possibly not as geophysically robust than the basic formulation, and that can degrade the model compliance to the geomagnetic field (see for instance the higher χ^2 value of model 4 when compared to model 2 in Table 1). In the present case, the best model would probably be model 3 as it invokes a simple and reasonable additional ingredient to clearly improve on the insufficient treatment of the zonal flow in model 2, while providing a magnetic field output which is even more compliant to the geomagnetic field than that of model 2. The hemispherical flow pattern can then be left as a perturbation in the inversion.

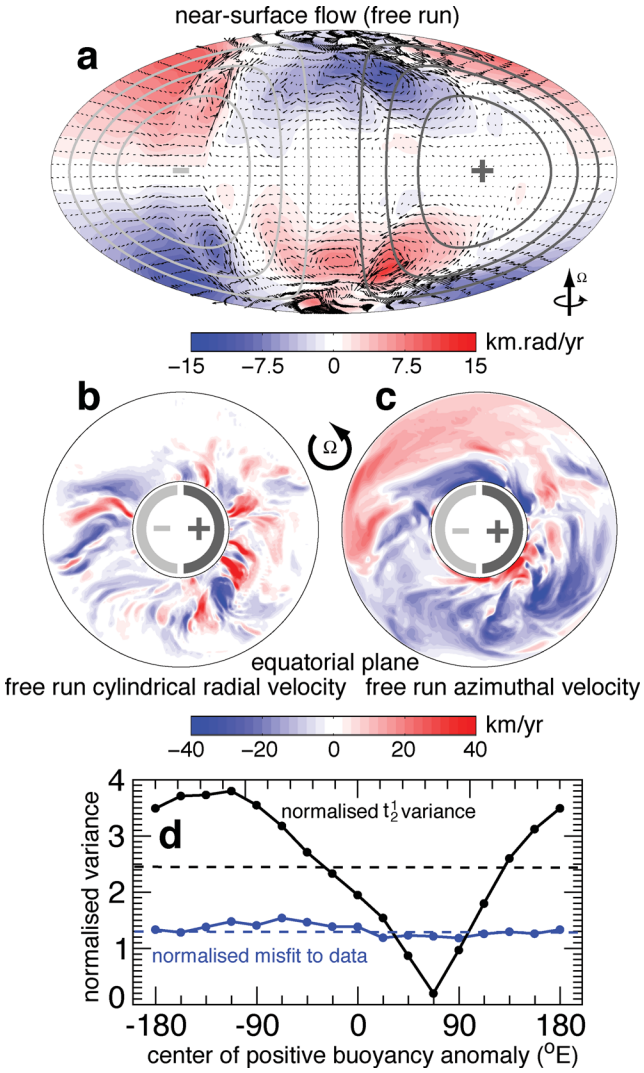

Figure 14. Direct and inverse modelling of flow resulting from a hemispherical inner-core buoyancy release (prior model 4). (a) Near-surface flow Hammer projection (same conventions as Fig. 7a), (b), (c) maps of the radial and azimuthal velocity field in the equatorial plane (same conventions as Figs 7b and c), from a direct numerical simulation (a free run unconstrained by the data) of model 4. In (a), (b), (c), the grey marks locate the positive and negative buoyancy anomalies superimposed on the homogeneous buoyancy release. (d) Normalized misfit to the data Δ_d and normalized variance of the t_2^1 spectral flow coefficient obtained in inversions of gufm-sat-Q3 for 2001 using model 4, as a function of the central longitude of the positive buoyancy anomaly. Values previously obtained in Fig. 9 with the homogeneous prior are reported as dashed lines.

The final remark concerns the interesting prospects opened by the compatibility between 3-D inverse geodynamo modelling and quasi-geostrophic core flow inversions. As mentioned in the introduction, the strengths and weaknesses of both approaches being complementary, forthcoming efforts in the attempt of building a physically sound geomagnetic data assimilation scheme (this work being considered as one of the steps) should include a combination of the two, in order to expand the time scale range over which the geomagnetic secular variation can be accounted for. Future work also includes a regularization of the inversions in time (in addition to space as presently done), and the buildup of a sequential assimilation scheme in time (as already undertaken in Aubert & Fournier 2011).

ACKNOWLEDGMENTS

JA wishes to thank Ingo Wardinski and an anonymous referee for insightful reviews. This work was supported by programs PNP/SEDI-TPS of French *Institut National des Sciences de l'Univers* (INSU) of CNRS, and by the French Agence Nationale de la Recherche under the grant ANR-2011-BS56-011. Numerical computations were performed at S-CAPAD, IPGP, France and using HPC resources from GENCI-IDRIS (Grants 2011-042122 and 2012-042122). This is IPGP contribution 3345.

REFERENCES

Alboussiere, T., Deguen, R. & Melzani, M., 2010. Melting-induced stratification above the Earth's inner core due to convective translation, *Nature,* **466**(7307), 744–747.

Amit, H., Olson, P. & Christensen, U., 2007. Tests of core flow imaging methods with numerical dynamos, *Geophys. J. Int.,* **168**(1), 27–39.

Aubert, J., 2005. Steady zonal flows in spherical shell dynamos, *J. Fluid. Mech.,* **542,** 53–67.

Aubert, J. & Dumberry, M., 2011. Steady and fluctuating inner core rotation in numerical geodynamo models, *Geophys. J. Int.,* **184**(1), 162–170.

Aubert, J. & Fournier, A., 2011. Inferring internal properties of Earth's core dynamics and their evolution from surface observations and a numerical geodynamo model, *Nonlin. Process. Geophys.,* **18**(5), 657–674.

Aubert, J., Aurnou, J. & Wicht, J., 2008. The magnetic structure of convection-driven numerical dynamos, *Geophys. J. Int.,* **172,** 945–956.

Aubert, J., Labrosse, S. & Poitou, C., 2009. Modelling the palaeo-evolution of the geodynamo, *Geophys. J. Int.,* **179**(3), 1414–1428.

Bloxham, J. & Jackson, A., 1991. Fluid flow near the surface of Earth's outer core, *Rev. Geophys.,* **29**(1), 97–120.

Buffett, B.A., 2010. Tidal dissipation and the strength of the Earth's internal magnetic field, *Nature,* **468**(7326), 952–955.

Buffett, B.A. & Glatzmaier, G.A., 2000. Gravitational braking of inner-core rotation in geodynamo simulations, *Geophys. Res. Lett.,* **27**(19), 3125–3128.

Busse, F.H., 1970. Thermal instabilities in rapidly rotating systems, *J. Fluid. Mech.,* **44**(3), 441–460.

Christensen, U. & Aubert, J., 2006. Scaling properties of convection-driven dynamos in rotating spherical shells and application to planetary magnetic fields, *Geophys. J. Int.,* **117,** 97–114.

Christensen, U. & Olson, P., 2003. Secular variation in numerical geodynamo models with lateral variations of boundary heat flux, *Phys. Earth planet. Int.,* **138,** 39–54.

Christensen, U. & Tilgner, A., 2004. Power requirement of the geodynamo from ohmic losses in numerical and laboratory dynamos, *Nature,* **429,** 169–171.

Christensen, U.R., 2011. Geodynamo models: Tools for understanding properties of earth's magnetic field, *Phys. Earth planet. Int.,* **187,** 157–169.

Christensen, U.R., Wardinski, I. & Lesur, V., 2012. Timescales of geomagnetic secular acceleration in satellite field models and geodynamo models, *Geophys. J. Int.,* doi:10.1111/j.1365-246X.2012.05508.x.

Christensen, U.R., Aubert, J. & Hulot, G., 2010. Conditions for Earth-like geodynamo models, *Earth. planet. Sci. Lett.,* **296**(3-4), 487–496.

Dormy, E., Cardin, P. & Jault, D., 1998. MHD flow in a slightly differentially rotating spherical shell, with conducting inner core, in a dipolar magnetic field, *Earth. planet. Sci. Lett.,* **160**(1-2), 15–30.

Finlay, C., Jackson, A., Gillet, N. & Olsen, N., 2012. Core surface magnetic field evolution 2000-2010, *Geophys. J. Int.*.

Finlay, C.C., Dumberry, M., Chulliat, A. & Pais, M.A., 2010. Short timescale core dynamics: theory and observations, *Space. Sci. Rev.,* **155**(1-4), 177–218.

Fournier, A. *et al.*, 2010. An Introduction to data assimilation and predictability in geomagnetism, *Space. Sci. Rev.,* **155**(1-4), 247–291.

Fournier, A., Aubert, J. & Thébault, E., 2011. Inference on core surface flow from observations and 3-D dynamo modelling, *Geophys. J. Int.,* **186**(1), 118–136.

Gillet, N., Pais, M.A. & Jault, D., 2009. Ensemble inversion of time-dependent core flow models, *Geochem. Geophys. Geosys.,* **10**(Q06004), doi:10.1029/2008GC002290.

Gillet, N., Jault, D., Canet, E. & Fournier, A., 2010. Fast torsional waves and strong magnetic field within the Earth's core, *Nature,* **465**(7294), 74–77.

Holme, R., 2007. Large-scale flow in the core, in *Treatise on Geophysics,* Vol. 8: Core Dynamics, ed. Olson, P., p. 107–130, Elsevier, Amsterdam.

Jackson, A., Bloxham, J. & Gubbins, D., 1993. Time-dependent flow at the core surface and conservation of angular momentum in the coupled core-mantle system, in *Dynamics of the Earth's Deep Interior and Earth Rotation,* Vol. 72, pp. 97–107, eds Le Mouël, J.-L., Smylie, D.E. & Herring, T., AGU Geophysical Monograph, Washington, DC.

James, R., 1973. Adams and Elsasser dynamo integrals, *Proc. R. Soc. Lond., A,* **331**(1587), 469–478.

Jault, D., 2008. Axial invariance of rapidly varying diffusionless motions in the Earth's core interior, *Phys. Earth planet. Int.,* **166**(1-2), 67–76.

Jault, D., Gire, C. & Le Mouël, J.-L., 1988. Westward drift, core motions and exchanges of angular momentum between core and mantle, *Nature,* **333,** 353–356.

Lhuillier, F., Fournier, A., Hulot, G. & Aubert, J., 2011. The geomagnetic secular-variation timescale in observations and numerical dynamo models, *Geophys. Res. Lett.,* **38**(L09306), doi:10.1029/2011GL047356.

Monnereau, M., Calvet, M., Margerin, L. & Souriau, A., 2010. Lopsided Growth of Earth's Inner Core, *Science,* **328**(5981), 1014–1017.

Moon, W., 1979. Numerical evaluation of geomagnetic dynamo integrals (Elsasser and Adams-Gaunt integrals)., *Comp. Phys. Comm.,* **16**(2), 267–271.

Mound, J.E. & Buffett, B.A., 2006. Detection of a gravitational oscillation in length-of-day, *Earth planet. Sci. Lett.,* **243**(3-4), 383–389.

Olson, P. & Aurnou, J., 1999. A polar vortex in the Earth's core, *Nature,* **402**(6758), 170–173.

Olson, P. & Christensen, U., 2002. The time averaged magnetic field in numerical dynamos with non-uniform boundary heat flow, *Geophys. J. Int.,* **151,** 809–823.

Olson, P. & Deguen, R., 2012. Eccentricity of the geomagnetic dipole caused by lopsided inner core growth, *Nat. Geosci.,* **5,** 565–569.

Olson, P., Christensen, U. & Driscoll, P., 2012. From superchrons to secular variation: a broadband dynamo frequency spectrum for the geomagnetic dipole, *Earth. planet. Sci. Lett.,* **319-320,** 75–82.

Pais, M.A. & Jault, D., 2008. Quasi-geostrophic flows responsible for the secular variation of the Earth's magnetic field, *Geophys. J. Int.,* **173**(2), 421–443.

Rau, S., Christensen, U., Jackson, A. & Wicht, J., 2000. Core flow inversion tested with numerical dynamo models, *Geophys. J. Int.,* **141**(2), 485–497.

Roberts, P.H. & Scott, S., 1965. On the analysis of the secular variation. I: a hydromagnetic constraint: theory, *J. Geomag. Geoelectr.,* **17,** 137–151.

Sabaka, T., Olsen, N. & Purucker, M., 2004. Extending comprehensive models of the Earth's magnetic field with Orsted and CHAMP data, *Geophys. J. Int.,* **159**(2), 521–547.

Sreenivasan, B. & Jones, C., 2005. Structure and dynamics of the polar vortex in the Earth's core, *Geophys. Res. Lett.,* **32**(20).

Sumita, I. & Olson, P., 1999. A laboratory model for convection in earth's core driven by a thermally heterogeneous mantle, *Science,* **286**(5444), 1547–1549.

Whaler, K.A., 1986. Geomagnetic evidence for fluid upwelling at the core-mantle boundary, *Geophys. J. R. astr. Soc.,* **86**(2), 563–588.

APPENDIX A: A MODEL RESOLUTION MATRIX

The model resolution matrix $\mathbf{K}_{fs}\mathbf{M}$ (Fig. A1) indicates how much of a given near-surface flow is recovered after successive execution of the direct and the inverse problems. Alternatively, this matrix also indicates whether the determination of a given flow coefficient relies entirely on the data or also requires knowledge of the prior and of other flow coefficients. For a fully determined inverse problem, every coefficient is perfectly resolved and $\mathbf{K}_{fs}\mathbf{M}$ is the identity matrix. Here, however, given the data resolution and the specified error, a perfect recovery of the flow coefficients is not expected, especially beyond spherical harmonic degree 13.

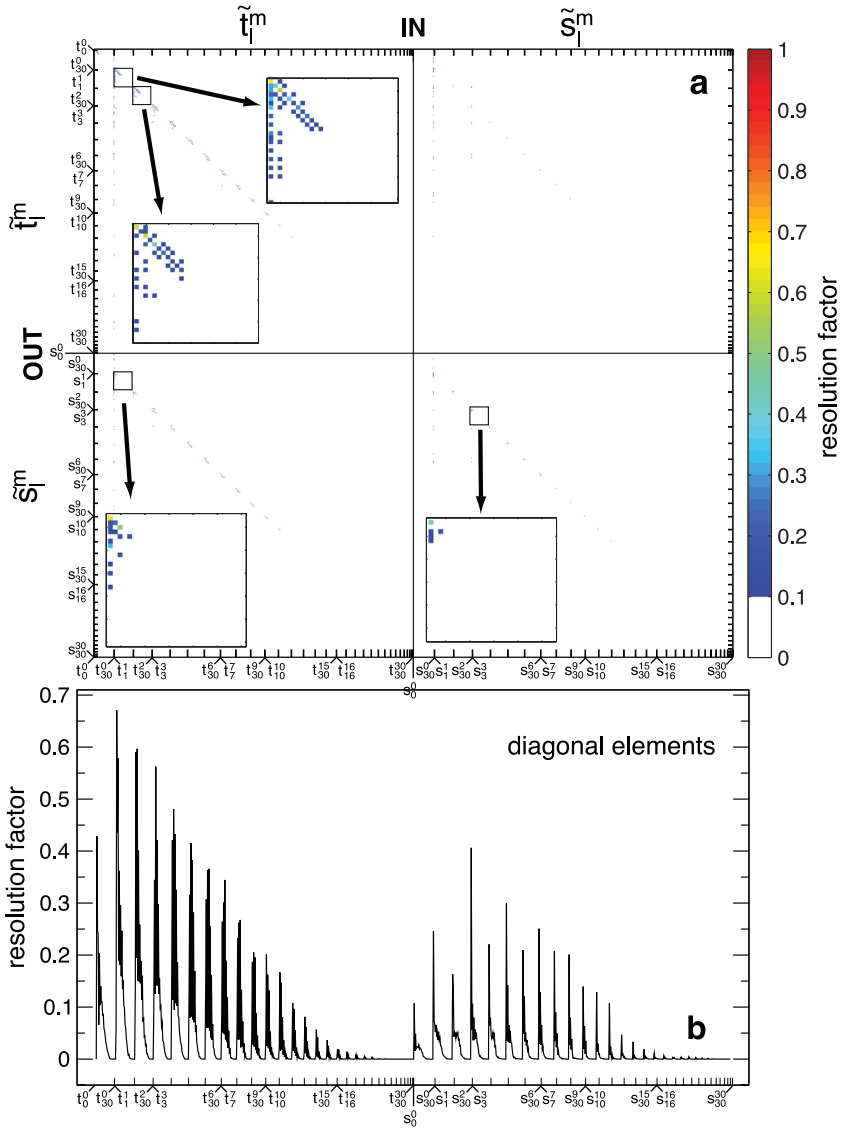

Figure A1. Model resolution matrix $\mathbf{K}_{fs}\mathbf{M}$ for the 2001 near-surface flow inversion of Fig. 12 (using prior model 3). (a) Full matrix, (b) diagonal coefficients.

In the case of the model 3 inversion presented in Fig. 12, the resolution (diagonal coefficients in Fig. A1a, also reported in Fig. A1b) is above 0.5 for toroidal flow coefficients with spherical harmonic order between 1 and 6, or half the data truncation. This can be considered satisfactory given the large underdetermination of the problem. The zonal flow (toroidal order 0) is a notable exception, with resolution coefficients at or below 0.4. The inversions presented in Figs 7 and 12 have already underlined the decisive influence of the prior in determining the zonal flow. As their inverted columnar flows have significant energies at harmonic orders 5–6, we expect these to be correctly resolved.

These results contrast with the good recovery obtained up to degree 13 in the twin experiments presented in Fig. 5. For that synthetic case, presumably, the perfect statistical compatibility between the prior and the searched flow solution is responsible for this extended recovery range.

The weak diagonal coefficients in the lower right-hand side corner of the resolution matrix, together with the presence of off-diagonal coefficients in the lower left-hand side corner, indicate that the determination of the spheroidal (upwelling) flow coefficients relies on the prior and on their correlation with the toroidal flow coefficients.

For all coefficients, the determination of flow coefficients beyond degree 6 relies on the prior to an increasing extent as the spherical harmonic degree increases.